Identification and validation of a 3D beam model of multi-stranded cables with a quasi-static robotic manipulation

Emmanuel Cottanceau, Olivier Thomas, Philippe Veron, Marc Alochet, Renaud Deligny

Identification and validation of a 3D beam model of multi-stranded cables with a quasi-static robotic manipulation

Emmanuel Cottanceau, Olivier Thomas, Philippe Véron, Marc Alochet,

Renaud Deligny

February 10, 2019

Abstract

This paper focuses on experimental validation and investigation of the validity of a 3D beam model for representing the assembly of flexible stranded cables in automotive industry. For this purpose, an original test bench has been designed. It allows quasi-static manipulation of cables with a robotic arm and retrieval of the cables 3D centerline position with a system of cameras. Investigation is carried out in three parts. Firstly, the beam parameters are identified with a single buckling test set up on the bench. Along with buckling theory analytical developments, this test leads to homogenized bending and shearing stiffness parameters. The torsional stiffness is estimated from the shearing parameter and cables measurement. Axial stiffness is calculated from the composite theory. Then, other loading experiments are performed. The results of the latter experiments are compared to numerical simulations based on a geometrically exact beam model and using both the identified beam parameters and the initial geometry of the cables as inputs. Lastly, a numerical analysis of the effects on the final geometry of uncertainties, for both identified parameters and initial geometry, is performed. The whole process provides clues on the validity of beam models for representing stranded cables: it gives good results for the prediction of the final geometry and average results for the reaction forces ; torsional stiffness, bending stiffness and initial geometry seem as the most influential

parameters of the model ; a buckling test seems to be a viable mean for identifying cable parameters.

Keywords: *Stranded cables ; Parameter estimation ; Timoshenko beam model ; Shape prediction ; Shearing study*

1 Introduction

1.1 Context

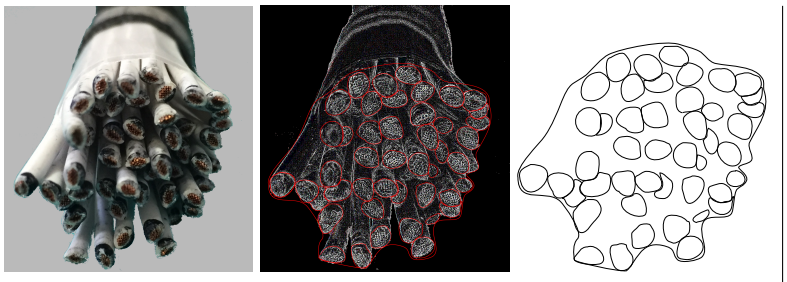

(a) Real cable (signal wires strand): picture of the cross-section on the left ; approximate reconstruction of the real cable cross-section (middle and right).

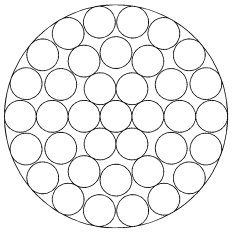

(b) Idealized (theoretical) stranded cable.

Figure 1: Cross-section of a stranded cable.

In automotive industry, it is necessary to simulate accurately and with fast computations the behavior of stranded or multi-stranded cables (figure 1) during an assembly operation. Because of the flexibility of electrical cables, large displacements/ rotations based physical models need to be developed. In this context, most of the current numerical tools are based on 3D geometrically exact beam models [Reissner, 1981, Irschik and Gerstmayr, 2011, Simo and Vu-Quoc, 1986].

These models assume rigidity of the cable cross-sections which are subjected to a particular kinematics justified by its slenderness. They lead to a great reduction of the number of degrees of freedom in comparison to full 3D models. This reduction leads to fast computations and still allows to describe very complex physical phenomena.
Depending on the chosen cross-sections kinematics, two main types of models compete against each other: models without shearing to which we will refer as Euler-Bernoulli models (EBM) and models with shearing to which we will refer as Timoshenko models (TM). The effect of shearing in a homogeneous beam is directly dependent of the thickness to length ratio of the beam: the thicker is the beam, the larger is the shearing deformation effect. As a result, for a very slender beam, the EBM is usually chosen. In addition, this method may lead to very fast algorithms [Bertails et al., 2006, Linn et al., 2008]. For a thick beam, the TM is usually preferred because it is physically more accurate.

Stranded cables are not homogeneous structures yet (see figure 1) and the type of models described above are theoretically not applicable for this purpose. The interested reader will consult for instance the outstanding review proposed by Spak et al. [Spak et al., 2013] to have a wide view of all stranded cables models such as the thin rod models [Huang, 1978, Sathikh et al., 1996] and the semi-continuous models [Raoof and Hobbs, 1988, Jolicoeur and Cardou, 1996]. This complex structure also involves another physical phenomenon not taken into account into the beam models: dry friction. This stick-slip phenomenon is evidenced by cyclic tests on stranded cables which show hysteretic behavior on the force-displacement diagram (see for instance experimental results of [Yu, 1949]). A lot of analytical models have been designed to take this effect into account, see for instance the review [Cardou and Jolicoeur, 1997] and the numerous references within, such as [Utting and Jones, 1987a, Utting and Jones, 1987b, LeClair and Costello, 1988]. Nevertheless, this effect leads to computationally costly algorithms and involves identifying additional frictional parameters. One of the goals of this paper is thus to evaluate if it is possible to neglect this phenomenon.
Indeed, one may assume that a stranded cable, as a whole structure, *behaves as* a homogeneous beam. In this case, the beam parameters are obtained by homogenization on the cross-section. With this method, and as advised by [Goodding et al., 2008], one may hope modeling the slipping between wires by shearing for example. The applicability of this homogenized beam model may however only be proved by experimental testing.

The above-mentioned beam parameters are 6 in number for the TM and 4 for

the EBM [Love, 1944]. They correspond to the stiffnesses for each generalized strain component. The 4 parameters in common to be determined are the axial stiffness EA, the torsional stiffness GJ and the bending stiffnesses in the two principal directions of the cross-section EI_2 and EI_3, in which (for a homogeneous beam) E is the Young's modulus, G the shear modulus, A the cross-sectional area and I_2, I_3 the second moments of area in the two principal directions. The two additional parameters of the TM are the shearing stiffnesses in the two principal directions GA_2 and GA_3, with A_2, A_3 being the shearing areas in the two principal directions.

The literature dedicated to the identification of these parameters is very dense for dynamical models [Castello and Matt, 2011, Spak et al., 2014], mainly developed for aeronautic applications [Ardelean et al., 2014] [Coombs et al., 2011]. The several methods of identification have been developed by supposing that a stranded cable has an idealized helicoidal structure made of a central wire (core), surrounded by layers of wire. Let us notice that this structure is adapted for structural cables but not very representative of automotive cables. Regardless, the methods of determination of the equivalent homogenized beam parameters may then be classified in two different categories: using cable measurement and material properties as input of a composite theory; experimental (and most of the time dynamical) testing.

The former method has the advantage of not requiring any costly experimental tests. However, it is based on a model which does not necessarily represent well the reality and thus does not allow a good accuracy. This type of method is thus more often used to narrow the properties in a theoretical range [Spak et al., 2014].

The experimental determination is often based on dynamical tests. For instance, among the existing experimental methods, let us mention the notable work of Goodding et al. [Goodding et al., 2011] in which the Young's modulus of the cable is determined by a static axial test while the shear modulus is obtained from curve fitting a FRF model on experimental transverse test data. Nevertheless, this method compels to design two different test benches. Besides, there also exist other techniques to determine the bending stiffness thanks to quasi-static bending tests such as the classic three point bending test or the work of Filiatrault and Stearn [Filiatrault and Stearns, 2005]. However, these methods do not give any information on the shearing stiffness.

As previously said, these methods have been set up for dynamical purposes in which the interest stands in the determination of the natural frequencies and the damping ratio. If the parameters are the same for dynamical models and quasi-static models, the studied outputs are different since the latters focus on the de-

formed shape of the cable and on the reaction forces at the boundaries. It is thus of great interest to see the efficiency of the identification for a quasi-static manipulation of cables. However, only few studies have been carried out for quasi-static purposes and the existing ones focus on completely different fields of applications, such as structural cables [Chen et al., 2015] and transmission line conductors [Papailiou, 1997] or give few insight on the physical model [Papacharalampopoulos et al., 2016]. By way of consequence, the literature lacks information on this topic.

1.2 Motivations and outline of the paper

In the context described above, we have devised a test bench in order to answer the following questions:

- Is it possible to simulate the quasi-static assembly of stranded cables with an homogenized equivalent beam model ?
- Is the shearing deformation relevant for modeling the potential slipping between the wires of the cables ? And, as a result, is the Timoshenko model more realistic than the Euler-Bernoulli model for modeling cables ?
- What parameters have a paramount importance in the predicted geometry and in the predicted reaction forces of the cables ?

To fulfill these purposes, it was straightforward to design a quasi-static loading experiment and fill the literature loophole. Taking advantage of the presence of a robotic arm in the laboratory, we have decided to use this device to apply step-by-step displacements/rotations to one extremity of samples of cables while the other is clamped. As the outputs of interest are the deformed shape of the cables and the evolution of the reaction forces, a force sensor is mounted on the robot and a vision system has been designed to get the 3D centerline of the cables. These data are used to perform a comparison to the numerical simulation developed in [Cottanceau et al., 2018].
As the test rig conceived is versatile and allows to perform several types of test (by means of the robotic arm), we have decided to also use it for the identification. Taking advantage of the closed-form expression of the transverse displacement as a function of the mechanical parameters for a buckling test, we thus propose a novel method for determining the beam parameters with only one test.
With that in hands, the experimental study is carried out with the following approach for several cables. The buckling test is performed and through the mathematical developments given in section 3, the mechanical parameters are identified

for both the EBM and the TM in section 4. Two other loading experiments presented in sections 5 and 6, referred as validation tests, are performed on the same cables and the deformed shapes and the reaction forces through the loading extracted. The identified parameters are used as inputs of the numerical algorithm which is run twice for each validation test: once with the EBM parameters and once with the TM parameters. Numerical and experimental results are finally compared. Finally, an experimental study on the influence of uncertainties of the mechanical parameters and of the initial geometry on the final geometry is carried out in section 7 and helps at commenting the experimental results. Synthesis of these results and further comments are provided as a conclusion in section 8.

2 Experimental setup

2.1 General description

	F_x, F_y	F_z	T_x, T_y, T_z
Sensing ranges	$\pm$330N	$\pm$990N	$\pm$30Nm
Resolution	1/8N	1/4N	10/1333Nm

Table 1: Force/torque sensor ATI Delta SI-330-30 characteristics.

The test bench, used for both identification of parameters and validation of the 3D beam model, is illustrated on Fig. 2. This bench is composed of two main parts: one for manipulating the cable and one for determining the 3D position of the cable.

On the first hand, a Staübli® TX90 6-axis robotic arm is equipped at its extremity with a 6-axis force sensor ATI® Delta SI-330-30 whose characteristics are given on Table 1. This sensor is connected to a National Instruments® data acquisition card whose data are read through the Matlab® Data Acquisition Toolbox. The numerical data obtained are the values of the 6 components of forces/torques with respect to time at a sampling rate of 2000 scans per second. These components are denoted $F_x(t)$, $F_y(t)$, $F_z(t)$, $T_x(t)$, $T_y(t)$ and $T_z(t)$ with F_i and C_i respectively representing the force reactions in direction i and the torque reactions around direction i, for i being one of the axis x, y or z represented on figure 2. The cable is attached to the robot through an interface which is linked to the force sensor (itself linked to the robotic arm). The other extremity of the cable is attached

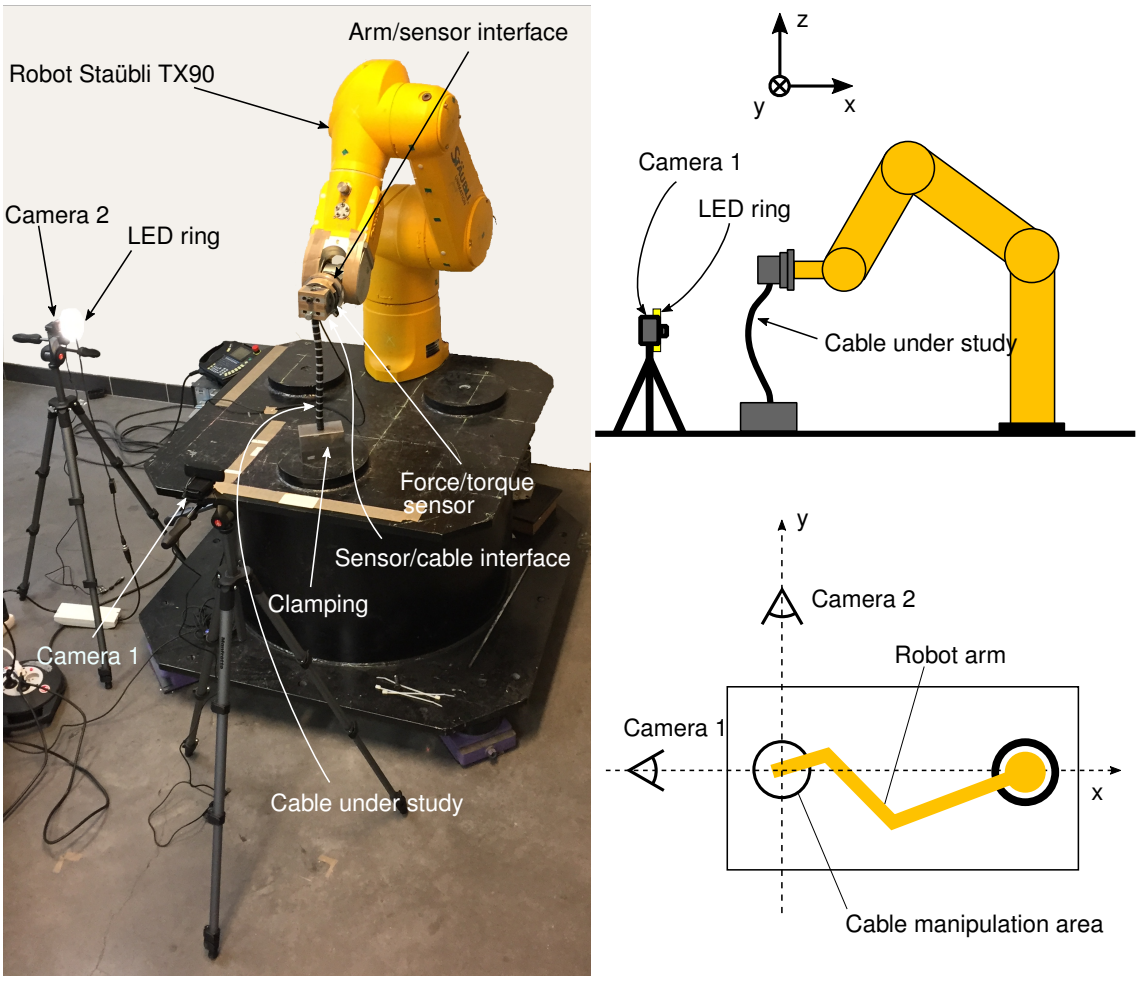

Figure 2: Illustration of the test bench and its various components: pictures with elements description (left), schematic representation of the bench from the right side (top right) and from above (bottom right).

to the robot platform through a second interface. Both interfaces, which follows the same principle, have been designed so that rotations nor translations are allowed (see Fig. 3): the fixation consists in a cylindrical hole of 18mm-diameter machined in a metallic part and in which the cable is tucked while two lateral cap screws squeeze the cable into the hole. The test boundary conditions are thus a clamping of one end and a prescribed 3D displacement/rotation of the other end. The prescribed displacement/rotation is applied by defining the trajectory of the

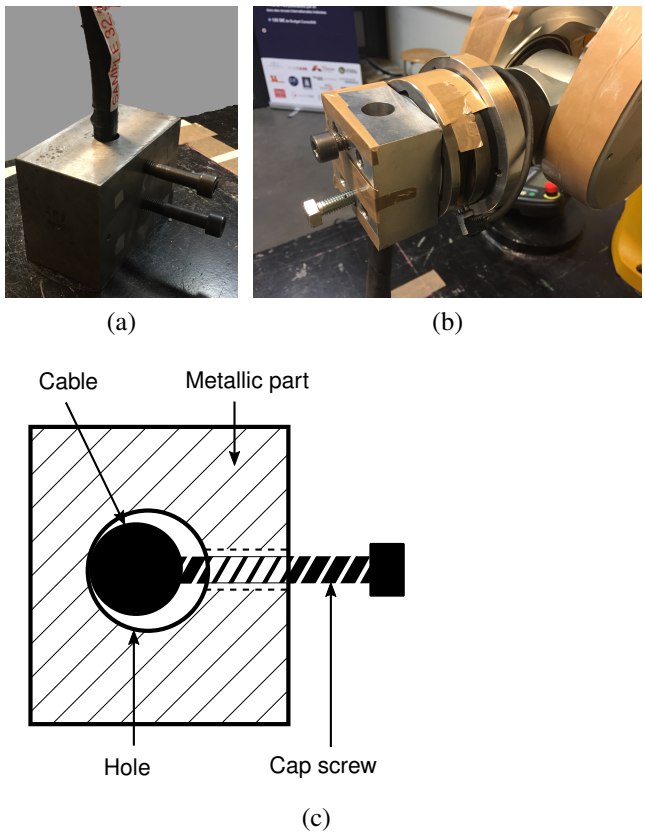

Figure 3: Fixation system: pictures of the robot platform interface (a) and of the robot tip interface (b) ; schematic representation of the interface functioning principle (c).

robot extremity through the robot software. The trajectory is decomposed in several steps of equal displacement/rotation increment: for each one of these steps, the robot applies the displacement/rotation increment and then makes a (motionless) pause of 5 s before resuming the motion at the next step. This step-wise motion is necessary to synchronize the force sensor data and the displacement obtained from vision system (robot controllers are not used as inputs of the experiment).

On the second hand, a vision system has been set up to recover the 3D centerline of the cable at each increment of displacement/rotation. This system is made up of two numerical cameras Logitech® HD Pro Webcam C920 mounted

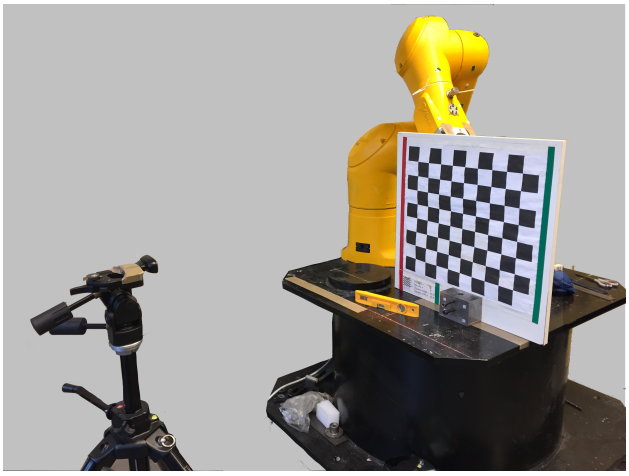

Figure 4: Illustration of the calibration of camera 2 with a checkerboard.

on two tripods and disposed perpendicularly as illustrated on Fig. 2. As a first step, the two cameras are calibrated one after the other to insure the perpendicularity of their optical axis as well as their right orientation. For the calibration, a checkerboard is positioned vertically in the cable manipulation area (Fig. 4). By means of the Matlab® Computer Vision System Toolbox, the square corners of the checkerboard are detected and the camera orientation is tuned so that its optical axis is normal to the plane of the checkerboard and so that it is horizontally aligned with the checkerboard. The checkerboard is then moved and positioned perpendicularly to its first position (still in the cable manipulation area and vertically). The calibration is then repeated for the second camera. This calibration aims at simplifying the mapping from the 3D object (the cable) to the 2D images captured by the cameras. Thereby, neglecting the distortion effects and as a first order calibration, the distances in the camera images are linearly related to the distances in the cable plane. The linear coefficient linking the pixel size in the cable plane to its real size is calculated through a second calibration step for each camera. Finally, from the data of the two perpendicular cameras, the 3D position of any point in the cable manipulation area may be reconstructed. Besides, several reflective tapes are stuck regularly along the centerline of each cable, with a distance of around 20 mm between each tape (see Fig. 5). A LED ring oriented toward the cable is fastened on each camera and lights up the reflective tapes. Image processing performed through a C++ program based on the Computer Vision System toolbox OpenCV [Ope, 1999] allows to detect each lightened reflective

tape on the cable and to find their centroid position (see Fig. 5). As aforementioned, the 3D positions of these points is found from the data of both cameras. Hence, the centerline may be reconstructed by interpolating these experimental points with cubic splines.

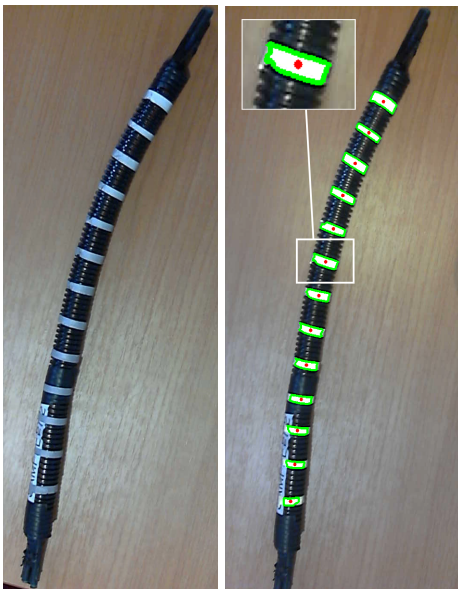

Figure 5: Camera centerline detection: view of the cable with reflective tapes from the camera (left); view of the cable after camera processing - green line around the tape detected and red point at the centroid (right).

2.2 Bench features

This original test bench exhibits several attractive features. Firstly, it allows a quasi-static manipulation of electrical cables whereas most tests on such cables are dynamical tests, as explained in introduction. Besides, a robotic arm allows to apply incrementally combination of rotations and translations in a 3D space. This versatility implies that a lot of different tests may be applied on this same bench, unlike most test benches which are very unidimensional. In addition, as a robotic arm is thought as a human arm, the trajectory applied to the extremity of the cable may be very human-like. It is then possible to carry out experiments very close to the human assembly of a cable. Finally, for well-chosen tests (without image

covering) our vision system allows to build the full 3D position of the centerline, whereas most experiments only give 2D positions.

3 Identification method on a buckling test: theory

3.1 General methodology

As already mentioned in introduction (section 1), the 3D beam model requires 6 input mechanical parameters: the axial stiffness EA, the bending stiffnesses EI_2, EI_3, the torsional stiffness GJ and the shearing stiffnesses GA_2, GA_3. The geometry of the stranded cables cross-section leads to the fair approximation of an idealized circular and symmetrical cross-section such as illustrated in figure 1b, which conducts to the further assumption of equality of the parameters $EI_2 = EI_3 = EI$ and $GA_2 = GA_3 = GA$ in the two principal directions of the cross-section. The identification then comes down to 4 parameters which depict the stiffness for each of the three following deformation modes:

- tension/compression for EA,
- bending for EI and GA,
- torsion for GJ.

As a result, three distinct identification tests should be carried out for the full determination of the parameters. However, as a cable is very stiff in the axial direction and that pulling is proscribed during an assembly operation, the axial stiffness EA is not preponderant in the numerical simulation and hence is easily reckoned from material and geometrical properties. For this parameter, following the approach of Spak et al. [Spak et al., 2014], the cable is supposed to be a composite made of parallel fibers in a concentric matrix and the equivalent Young's modulus is thus calculated with the formula [Sendeckyj, 2016]:

$$E = V_f E_f + V_m E_m + \frac{2(\nu_f - \nu_m)^2 (1-\nu_f) E_m V_f E_f}{(1-V_m) E_m (1-\nu_f - 2\nu_f^2) + E_f ((1-\nu_m - 2\nu_m^2) V_m + (1+\nu_m))}, \tag{1}$$

with indices f and m representing the fiber and the matrix values respectively, $V_\bullet$ being the volume fraction, $E_\bullet$ the Young's modulus and $\nu_\bullet$ the Poisson's ratio. This formula is a modified rule of mixture for a cylindrical fiber-reinforced

composite which takes into account the dilatation/contraction of the fibers in the transverse direction due to the axial elongation/compression [Hill, 1964]. The expression (1) is then multiplied by the maximal cross-sectional area $A_{\max} = \pi R^2$, R being the radius of the cable, to obtain the axial stiffness.

Taking advantage of the versatility offered by our test bench for applying several types of displacements/rotations, we have set up a buckling test for evaluating the bending behavior of the cables. The 2D theory of buckling for the Timoshenko model indeed links both EI and GA to the critical buckling load and the transverse displacement. Likewise, the buckling theory for the EBM relates the two last quantities to EI. As a result, we propose here a novel method to determine the coefficients characterizing the bending behavior of cables using a single test for both the EBM and the TM. The theoretical developments necessary to understand the process of identification are presented in the next section. At the same time, the parallel is made between the EBM and the TM by stating the main differences between each one of the models and thereby well understanding the stakes of choosing one or the other method.

The last parameter GJ is usually reckoned through a torsion test. However, according to the designed bench, such a test revealed difficult to set up for two reasons: the fixation system (Fig. 3) is not adapted to pure torsion (slipping between the wires and the protection is likely to occur) and the vision system does not allow to measure the variation of twist angle. To avoid designing another setup, we have thus decided to simply evaluate the torsional stiffness GJ from the identified GA and its geometrical properties. For a homogeneous TM beam, the torsional stiffness is related to the shearing stiffness by

$$GJ = \frac{GA}{A_{\max}} J_{\max}, \tag{2}$$

with $J_{\max} = \pi \frac{R^4}{2}$ being the maximal polar second moment of area. As a first order approximation, this formula has been transposed to our cable model. In addition, as one of the study prime interests is to determine the influence of the shearing, the same torsional stiffness is used for the EBM so that the comparison is only focused on the shearing.

3.2 Buckling theory of an Euler-Bernoulli beam and a Timoshenko beam

Within the framework of the 2D buckling theory, an initially perfectly straight homogeneous beam of length L subjected to an axial compressive load P is con-

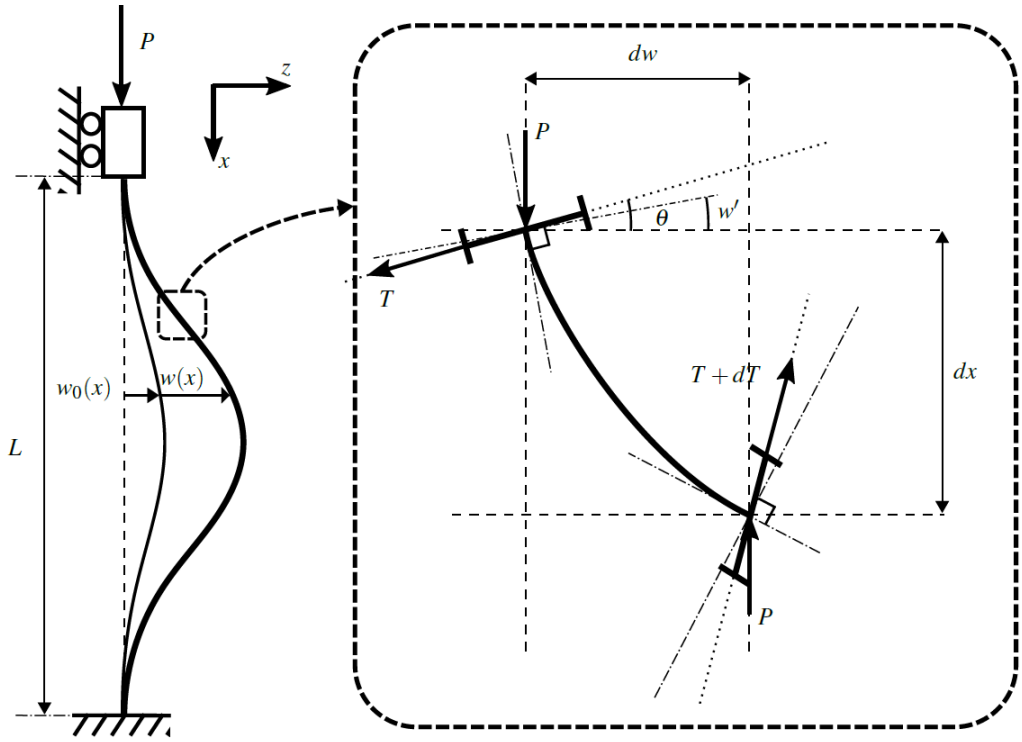

Figure 6: Buckling of a clamped-clamped Timoshenko beam: schematic representation and notations.

sidered (see Fig. 6). Under this load, the beam fails and undergoes a transverse deflection w. The calculations are developed for the deformed shape of the beam (after buckling) at 2$^{\text{nd}}$ order (moderate rotations hypothesis) and leads, for a perfect TM beam, to the governing equations [Bažant and Cedolin, 2010]

$$\begin{aligned} &\theta'''(x) + \frac{P}{EI}\left(1 + \frac{P}{GA}\right)\theta'(x) = 0, \\ &w'(x) = \theta(x) - \frac{EI}{GA+P}\theta''(x), \end{aligned} \tag{3}$$

where the transverse displacement w and the angle of rotation of the cross-section θ are the unknowns of the problem which depend solely on the abscissa along the beam x. EI is the bending stiffness and GA is the shearing stiffness. Depending on the shearing force used for defining the shearing stiffness, this latter coefficient may have different values (see [Bažant and Cedolin, 2010], pp. 34). Let us point

out that the shearing force used here is the one of the geometrically exact beam model [Cottanceau et al., 2018], that being the force contained in the plane of the cross-section and not necessarily normal to the centerline, T (see Fig. 6). The prime symbol $'$ denotes the derivative with respect to x.
In absence of shearing, the shearing coefficient GA tends toward infinity and equation (3b) becomes $\theta(x) = w'(x)$, which reads as the cross-sections remaining normal to the centerline along the deformation. In that case, introducing (3b) in (3a) simplifies in

$$w''''(x) + \frac{P}{EI} w''(x) = 0, \tag{4}$$

which is the equation governing the buckling of a EBM beam. Solving these equations for a clamped-clamped beam, i.e with the boundary conditions $w(0) = w(L) = 0$ and $w'(0) = w'(L) = 0$ for the EBM and $\theta(0) = \theta(L) = 0$ for the TM leads to the respective critical forces

$$P_{\text{cr}}^{\text{EB}} = \frac{4\pi^2 EI}{L^2}, \quad P_{\text{cr}}^{\text{T}} = \frac{GA}{2}\left(\sqrt{1 + 16\pi^2 \frac{EI}{GAL^2}} - 1\right). \tag{5}$$

In a real case, such as the experimental bench, the beam is not perfect. The theory of imperfect beams is herein developed solely for the TM, and the few important results are deduced for the EBM by making GA tend to infinity. The presence of an initial flaw $(w_0(x), \theta_0(x))$ is taken into account by replacing w and θ by $w + w_0$ and $\theta + \theta_0$ respectively in equation (3). It is assumed that initially there is no shearing so that $\theta_0(x) = w_0'(x)$. In addition, when the load P is equal to 0 the beam is undeformed and thus $w(x) = \theta(x) = 0$: introducing these hypotheses in equation (3) leads to $\theta_0''(x) = w_0'''(x) = 0$. Accounting for all these points leads to the imperfect TM beam governing equations

$$\begin{aligned} &\theta''' + \frac{P}{EI}\left(1 + \frac{P}{GA}\right)(\theta' + w_0'') = 0, \\ &w' = \theta - \frac{EI}{GA + P}\theta''. \end{aligned} \tag{6}$$

Now introducing the dimensionless variables

$$\bar{\theta} = \theta, \quad \bar{w} = \frac{w}{h} \quad \text{and} \quad \bar{x} = \frac{x}{L}, \tag{7}$$

in (6), with h being the characteristic length of the cross-section (diameter for a circular cross-section or thickness for a rectangular cross-section), one can write

the dimensionless equations governing the flawed beam (where the dependency in x has been dropped for simplicity)

$$\begin{aligned} &\bar{\theta}''' + \bar{k}^2\bar{\theta}' = -\alpha\bar{k}^2\bar{w}_0'', \\ &\bar{w}' = \frac{1}{\alpha}\bar{\theta} - \frac{\eta}{\alpha(1+\eta\bar{k}_0^2)}\bar{\theta}''. \end{aligned} \tag{8}$$

In equation (8) the following dimensionless characteristic parameters have been introduced:

$$\alpha = \frac{h}{L},\ \ \eta = \frac{EI}{GAL^2},\ \ \bar{k}_0^2 = \frac{PL^2}{EI},\ \ \bar{k}^2 = (1+\eta\bar{k}_0^2)\bar{k}_0^2 = \left(1+\frac{P}{GA}\right)\frac{PL^2}{EI}, \tag{9}$$

where α is the height to length ratio, η is the bending to shearing stiffness ratio, $\bar{k}_0$ the dimensionless wave number of an Euler-Bernoulli beam and $\bar{k}$ the dimensionless wave number of a Timoshenko beam. Among these parameters, η is of paramount importance in understanding the influence of shearing since it is the only parameter which depends on GA ($\bar{k}$ depends indirectly on GA through η). As a result, the Euler-Bernoulli model is obtained from the Timoshenko model by setting $\eta = 0$. Therefore, by applying $\eta = 0$ in the expressions (9) above, the characteristic parameters of the Euler-Bernoulli beam reduce to only α and $\bar{k}_0$ and the equilibrium equation of the imperfect EBM becomes simply

$$w'''' + \bar{k}_0^2 w'' = -\bar{k}_0^2 w_0''. \tag{10}$$

In the case of a clamped-clamped beam, one may decently assume that the initial deflection writes $\bar{w}_0(x) = \bar{a}_0\left(1-\cos(2\pi\bar{x})\right)/2$ with $\bar{a}_0 = a_0/h$ and a_0 being the magnitude of the initial flaw at the middle of the beam ($\bar{x} = 1/2$). The system (8) is a nonhomogeneous system of two linear differential equations with constant coefficients. Summing the general solution of the homogeneous system associated to (8) and a particular solution of the full system searched under the form $\big(w_P(x) = F\cos(2\pi x),\ \theta_P(x) = G\sin(2\pi x)\big),\ \ F, G \in \mathbb{R}$, gives the general solution of (8) depending on 4 real constants. These constants are determined with the 4 boundary conditions of a clamped-clamped beam $\bar{w}(0) = \bar{\theta}(0) = \bar{w}(1) = \bar{\theta}(1) = 0$ and leads to the solution

$$\begin{cases} \bar{w}(x) = \dfrac{\bar{a}_T}{2}\left(1-\cos(2\pi\bar{x})\right), \\ \bar{\theta}(x) = \bar{a}_T\dfrac{\pi\alpha(1+\eta\bar{k}_0^2)}{1+\eta\left(\bar{k}_0^2+(2\pi)^2\right)}\sin(2\pi\bar{x}). \end{cases} \tag{11}$$

In this equation, $\bar{a}_T$ is the maximal transverse displacement (in $\bar{x} = 1/2$) and writes as a function of the load P (implicitly, inside $\bar{k}_0$ and $\bar{k}$), of the initial flaw $\bar{a}_0$ and of the parameters of the problem:

$$\bar{a}_T(P, \bar{a}_0) = \bar{a}_0 \bar{k}_0^2(P) \frac{1 + \eta\left(\bar{k}_0^2(P) + (2\pi)^2\right)}{(2\pi)^2 - \bar{k}^2(P)}. \tag{12}$$

Consequently, it is noticed that for $P = 0$, $\bar{k}(0) = 0$ and thus $\bar{a}_T(0) = 0$.
Besides, for $\eta = 0$ (and $\bar{k} = \bar{k}_0$), the maximal displacement of a Euler-Bernoulli beam is deduced and equals

$$\bar{a}_{\mathrm{EB}}(P, \bar{a}_0) = \bar{a}_0 \frac{\bar{k}_0^2(P)}{(2\pi)^2 - \bar{k}_0^2(P)}. \tag{13}$$

3.3 Models comparison

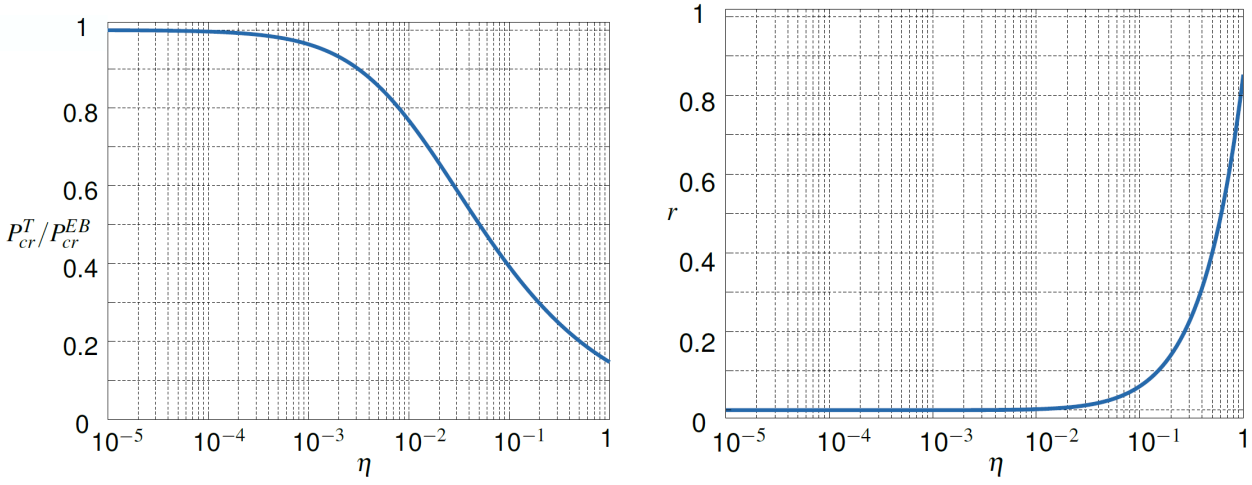

(a) (b)

Figure 7: Influence of the shearing on the critical force: (a) ratio of the TM critical force to the EBM critical force as a function of the shearing parameter η; (b) ratio of the partial derivatives with respect to GAL^2 and EI, $r = \left| \frac{\partial P_{\mathrm{cr}}^{\mathrm{T}}/\partial(GAL^2)}{\partial P_{\mathrm{cr}}^{\mathrm{T}}/\partial(EI)} \right|$, as a function of η.

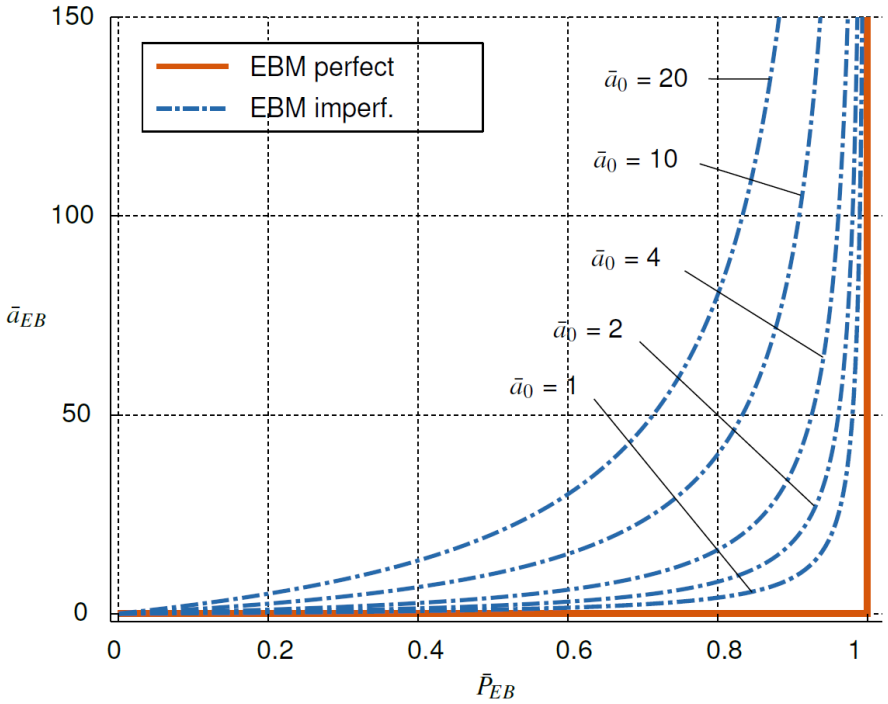

(a) EBM axial load vs. transverse displacement equilibrium curves for several values of the normalized initial deflection $\bar{a}_0$.

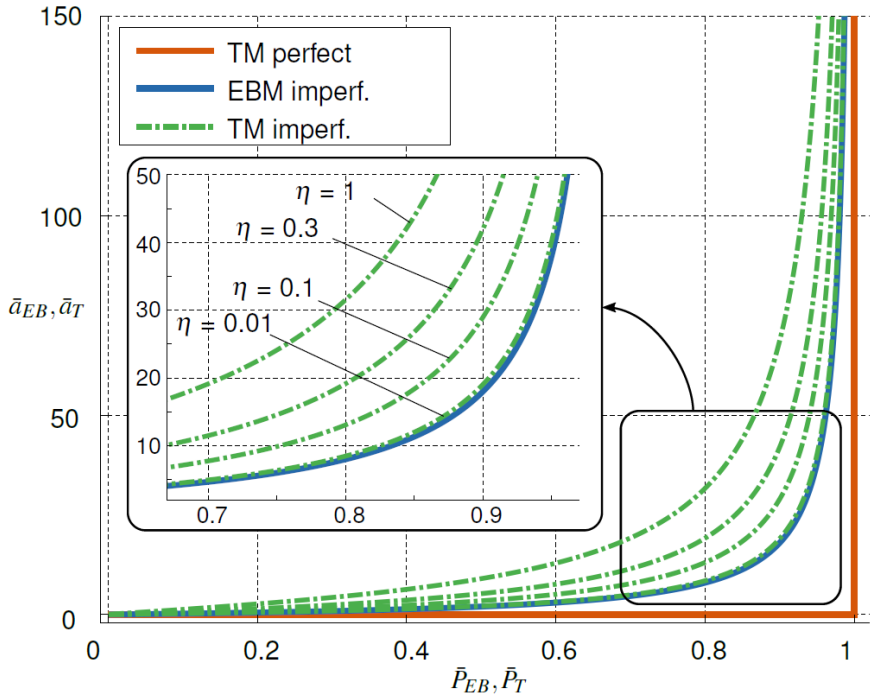

(b) TM axial load vs. transverse displacement equilibrium curves for several values of the shearing parameter η and a fixed initial deflection $\bar{a}_0 = 2$. The result is compared to the EBM equilibrium curve with the same $\bar{a}_0$.

Figure 8: Normalized equilibrium curves for the TM and the EBM and influence of the main parameters.

The model described above requires a few comments. The influence of shearing in the TM is observed first by studying the evolution of the critical load as a function of shearing stiffness. From formulas (5), one can write the ratio of TM to EBM critical loads as

$$\frac{P_{\text{cr}}^{\text{T}}}{P_{\text{cr}}^{\text{EB}}} = \frac{1}{8\pi^2\eta}\left(\sqrt{1+16\pi^2\eta}-1\right). \tag{14}$$

On figure 7(a), the evolution of this ratio with respect to η is depicted. One notices that for small values of η ($\eta < 10^{-4}$) the critical force is almost identical for both the EBM and the TM. For higher values ($\eta > 10^{-4}$), the influence of shearing becomes significant and the TM critical loads highly decrease for increasing η: for instance, for $\eta = 5 \cdot 10^{-2}$, the TM critical loads are twice smaller than the EBM critical load.
Then, to compare the influence of the stiffnesses GAL^2 and EI on the TM critical load, the ratio r of the partial derivatives of the critical load with respect to both these parameters is examined :

$$r = \left|\frac{\partial P_{\text{cr}}^{\text{T}}/\partial(GAL^2)}{\partial P_{\text{cr}}^{\text{T}}/\partial(EI)}\right| = \left|\eta - \frac{1}{8\pi^2}\left(\sqrt{1+16\pi^2\eta}-1\right)\right|. \tag{15}$$

The meaning of this ratio is easily understood by observing limit cases:

- $r \longrightarrow 0$ interprets as a null dependency of P_{cr}^{T} in GAL^2 with respect to EI: bending totally overrides shearing for influencing the critical load;
- $r = 1$ means that the variations of GAL^2 and EI equally influence the variation of P_{cr}^{T}: shearing and bending equivalently influence the critical load ;
- $r \longrightarrow \infty$ interprets as a null dependency of P_{cr}^{T} in EI with respect to GAL^2: shearing totally overrides bending for influencing the critical load.

The evolution of r as a function of η is exhibited on Fig. 7(b). When $\eta \ll 1$ this quantity becomes $r \approx 4\pi^2\eta^2$. This equation and the figure 7(b) thus demonstrates that, the more η is small, the more the influence of the shearing stiffness GAL^2 on the critical force is weak in comparison to EI. In a general manner, as η is usually lower than 1, the influence of GAL^2 is always smaller than the influence of EI ($r < 1$): by way of consequence, bending stiffness has a higher influence on the buckling load than shearing stiffness.

From the expression of the TM critical load (5), one may introduce the quantity γ which solely depends on the shearing parameter η and is defined by

$$\gamma(\eta) = \frac{P_{\text{cr}}^{\text{T}}}{GA} = \frac{1}{2}\left(\sqrt{1+16\pi^2\eta}-1\right). \tag{16}$$

Using this new variable and the normalized axial load $\bar{P}_T = \frac{P}{P_{\text{cr}}^{\text{T}}}$, the normalized transverse displacement $\bar{a}_T$ expressed in (12) comes

$$\bar{a}_T = -\bar{a}_0 \frac{\gamma(\eta)\bar{P}_T^2 + (1+\gamma(\eta)+\gamma^2(\eta))\bar{P}_T}{\gamma(\eta)\bar{P}_T^2 + \bar{P}_T - (1+\gamma(\eta))}. \tag{17}$$

Similarly, the normalized EBM transverse displacement (13) writes

$$\bar{a}_{\text{EB}} = \bar{a}_0 \frac{\bar{P}_{\text{EB}}}{1-\bar{P}_{\text{EB}}}, \tag{18}$$

with the normalized axial load $\bar{P}_{\text{EB}} = \frac{P}{P_{\text{cr}}^{\text{EB}}}$. The rewriting of these normalized quantities shows that the normalized transverse displacement depends only on the initial default $\bar{a}_0$ and on the shearing parameter η for the TM and only on the initial default $\bar{a}_0$ for the EBM. Plots of the TM and the EBM transverse displacement with respect to the applied axial load are depicted on figure 8 for several values of the parameters $\bar{a}_0$ and η. These curves show that the initial deflection softens the right angle of the perfect beam equilibrium curve: the change of slope due to buckling is more abrupt when the initial deflection is small and thus tends toward the perfect beam model when $\bar{a}_0$ tends toward 0. This interprets as a earlier buckling for a structure with initial deflection which hence is more sensitive to buckling phenomena. The shearing parameter in the TM has almost the same role, but the TM tends toward the EBM for a decreasing η and an identical initial deflection instead of the perfect model. The shearing thus add flexibility to the structure.

Besides, the 2^{nd} order TM buckling theory is also compared to the geometrically exact beam theory (GEBM) [Cottanceau et al., 2018] on figure 9. The equilibrium curves for several values of η show that the 2^{nd} order theory agrees with the exact theory on a large range of applied force and that the curves depart from each other when approaching the critical force value. The divergence starts becoming significant at around 95 % of the critical force value. After this point, the beam modeled with the geometrically exact theory becomes stiffer.

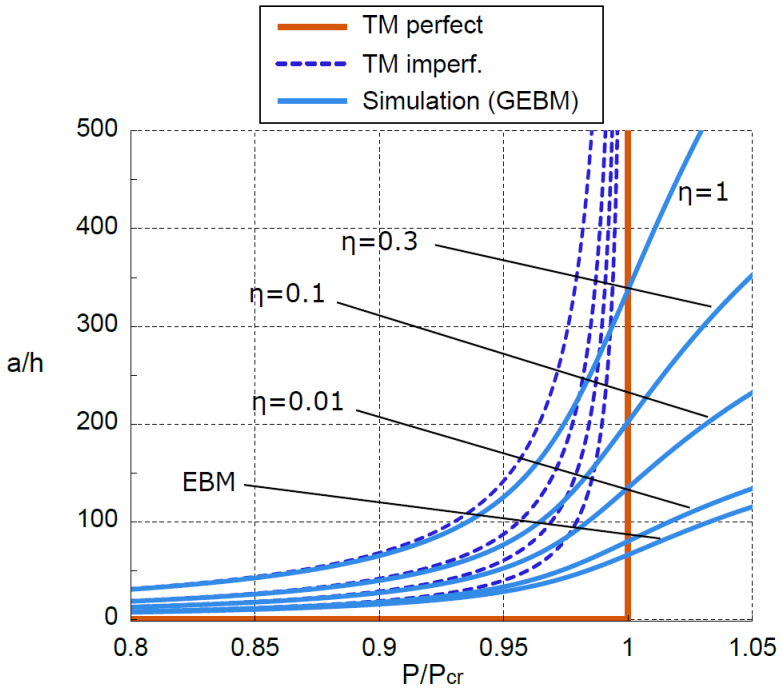

Figure 9: Normalized equilibrium curves for the simulation [Cottanceau et al., 2018] based on a geometrically exact beam model (TM). The results are presented for several values of η and compared to the 2nd order TM buckling theory.

3.4 Identification

As explained before, the identification process is based on the beam model with an initial flaw which is more realistic and allows fitting on experimental data.
For facilitating the optimization process of the TM, the TM transverse displacement (12) is first rewritten under the form

$$a_T = a_0 \frac{P}{P_0} \frac{1+\eta\left((2\pi)^2+\frac{P}{P_0}\right)}{(2\pi)^2-\left(1+\eta\frac{P}{P_0}\right)\frac{P}{P_0}} = a_0\, f_{\text{opt}}(P,P_0,\eta), \tag{19}$$

with $P_0 = \frac{EI}{L^2}$. Fitting the parameters $\bar{a}_0$, P_0 and η is carried out in the least-squares sense, using the experimental transverse displacement a_{exp} and the applied axial load P_{exp} as the observed outputs and inputs of the problem respec-

tively. The Optimization toolbox of Matlab® is used to run a multistart optimization on the fitting problem (19) based on the trust-region-reflective algorithm [Coleman and Li, 1996a, Coleman and Li, 1996b]. As the problem is linear into a_0, a splitting between the linear part and the nonlinear part f_{opt} is done, so that the optimization algorithm is only performed on P_0 and η. Indeed, at each iteration k of the optimization algorithm, candidate values of P_0 and η are tested, which we denote P_0^k and η^k. As a result, it comes from(19) that $a_{\text{exp}} = a_0\, f_{\text{opt}}(P_{\text{exp}}, P_0^k, \eta^k) = a_0\, f_{\text{opt}}^k$, with f_{opt}^k being a known coefficient at iteration k for any given value of P_{exp}. As a result a_0 is obtained at each step of the iterative process by linear regression.

The parameters P_0 and η are searched into the respective ranges $[0,\ 10^5]$ and $[10^{-8},\ 2.5 * 10^{-2}]$. From the parameters obtained after the optimization process, one deduces easily the material parameters $EI = P_0 L^2$ and $GA = \frac{P_0}{\eta}$.
For the EBM, the expression of the transverse displacement (18) is rewritten with the help of the expression (5)

$$\bar{a}_{\text{EB}} = \bar{a}_0 \frac{\frac{1}{4\pi^2}\frac{P}{P_0}}{1 - \frac{1}{4\pi^2}\frac{P}{P_0}}. \tag{20}$$

The Southwell plot method [Bažant and Cedolin, 2010] could have been used as identification method for the EBM. However, for keeping consistency in the identification process of the two methods, the same method as for the TM is used with, this time, an optimization focusing only on P_0 searched into the range $[0,\ 10^5]$.
An illustration of the experimental points and the corresponding fitted curves is provided on figure 10(b).

3.5 Optimization process testing

To determine the robustness of the optimization process developed in section 3.4, a reverse testing has been set up. For this purpose, 3 sets of mechanical parameters have been chosen, covering a range of η from 2.5 10^{-4} to 2.5 10^{-2}, and supplied in "theoretical" rows of table 2. With these data, the buckling test exhibited on figure 6 has been simulated with the beam simulation algorithm described in [Cottanceau et al., 2018]. From the simulation, the equilibrium curve representing the theoretical transverse displacement at the middle of the beam a_{th} as a function of the applied axial force P_{th} is obtained. Then, selecting and using 20

equidistant points on this curve which act as virtual experimental points, the optimization process of section 3.4 is launched for both the EBM and the TM. The identified beam parameters, which are EI, GA and a_0, are finally compared to the initially chosen parameters in table 2.
The results show that:

- The initial deflection is well predicted.
- The fitted mechanical parameters for the TM are very close to the theoretical values for a large η and drift apart when η decreases. This is very significant for the error on GA value and less for the error on EI value which is at worst of 9.3 % on the chosen tests.
- Conversely, the fitted bending stiffness for the EBM is very close to the theoretical values for a small η and drift apart when η increases.

These results match well with the fact that for a very stiff beam in shearing direction, GA has a lower influence on the buckling effect (figure 7), and by way of consequence is harder to identify with our model. Conversely, the results are very encouraging for a small shearing stiffness. For the EBM, the results are reversed since it is harder to fit a no-shearing model on a beam with a large shearing deformation with accuracy, while the algorithm behaves well for a beam with almost no shearing.

3.6 Example of identification

To check the reliability of our method, the identification process has been first tested on a ruler made of homogeneous steel and whose material and geometrical properties are provided in table 3. These data along with equation (5) lead to the TM critical load 42.5 N.
The test bench described in section 2 is used to apply the buckling test to the steel ruler (see Fig. 10(a)). Post-processing of the data given by the force sensor and the vision system gives the experimental axial force vs. transverse displacement equilibrium curves (Fig. 10(b)). Applying the identification method described in section 3.4, leads to beam parameters $EI = 45.56\ 10^{-3}$ Nm^2 and $GA = 23.4\ 10^3$ N for the TM and $EI = 45.47\ 10^{-3}$ Nm^2 for the EBM.
The value of the shearing stiffness is quite far from the expected value. However, as the ruler is very stiff in this strain direction (theoretical bending to shearing ratio $\eta_{\text{th}} = 1.39\ 10^{-6}$), the impact of GA on the reaction force is very small (as

		Timoshenko				Euler-Bernoulli	
		EI (N.m^2)	GA (N)	a_0 (mm)	η	EI (N.m^2)	a_0 (mm)
Test 1	Theoretical	1.018	367	2.0	$2.5\ 10^{-2}$	1.018	0.002
	Fitted	1.021	384	2.0	$2.44\ 10^{-2}$	0.64	2.4
	Relative error	**0.3**%	**4.8**%	**0.7**%	**4.3**%	**37**%	**20.9**%
Test 2	Theoretical	1.018	$3.67\ 10^3$	2.0	$2.5\ 10^{-3}$	1.018	2.0
	Fitted	1.022	$4.63\ 10^3$	2.0	$2.0\ 10^{-3}$	0.95	2.0
	Relative error	**0.4**%	**26.3**%	**0.4**%	**20.5**%	**6.5**%	**0.8**%
Test 3	Theoretical	1.018	$3.67\ 10^4$	2.0	$2.5\ 10^{-4}$	1.018	2.0
	Fitted	1.11	$4.82\ 10^3$	2.0	$2.1\ 10^{-3}$	1.032	2.0
	Relative error	**9.3**%	**86.8**%	**0.5**%	**732**%	**1.4**%	**1.0**%

Table 2: Optimization algorithm testing.

Material		**Cross-section**		**Length**	**Beam parameters**	
E	ν	w	h	L	EI	GA
203 GPa	0.33	18.1 mm	0.52 mm	200mm	$43.1\ 10^{-3}$ Nm^2	$718\ 10^3$ N

Table 3: Steel ruler geometrical and mechanical properties

demonstrated by figures 7(a)-(b) for small η). As a result, a high accuracy was not expected (see also section 3.5 for a discussion around this topic). Nevertheless, the identified GA is high (experimental $\eta_{\text{exp}} = 4.87\ 10^{-5}$) which is in accordance with the ruler shearing stiffness and we expect better accuracy for more flexible cables. The identified EI for the EBM and the TM are in agreement with each

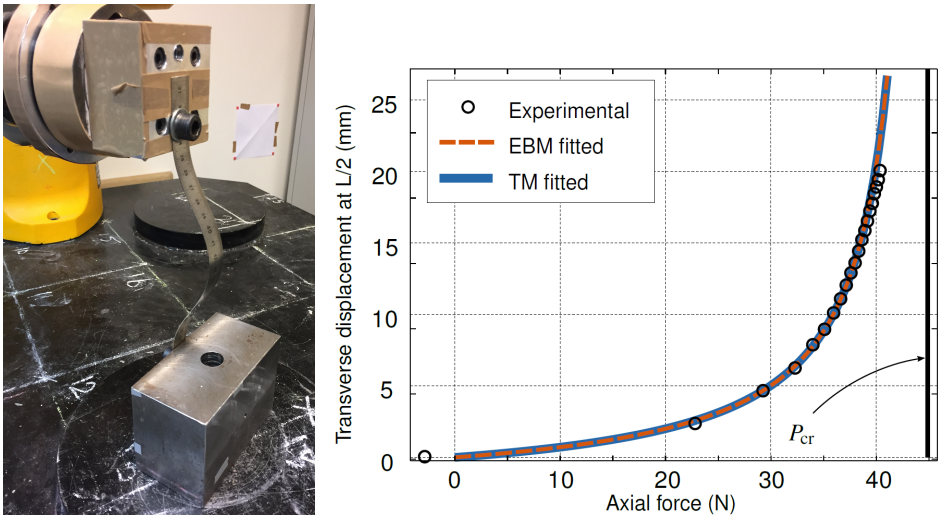

(a) (b)

Figure 10: Fitting of Euler-Bernoulli and Timoshenko curves on experimental data for a steel ruler: picture of the ruler during a test (left); experimental and fitted curves (right).

other and the error with respect to the theoretical value is around 6%. It thus proves the fidelity of this identification for the bending modulus.

4 Identification method on a buckling test: experimental results

4.1 Cables under study

The whole identification process described in section 3 is here applied to 5 samples of cables. These samples, representative of the stranded cables that can be found in automotive industry and pictured figure 11 will serve as a basis for all the experimental results presented in this section and the following.
The samples that we will denote from 1 to 4 are made of 50 signal wires whose core is made up of 18 annealed copper filaments of Young's modules $E_{cu} =$ 120GPa and Poisson ratio $\nu_{cu} = 0.33$ surrounded by an insulating elastomer of polypropylene (PP) of Young's modulus $E_{PP} =$ 1GPa and Poisson ratio $\nu_{PP} =$ 0.42. The filaments diameter is equal to $d^1_{cu} = 220\mu$m, the core diameter is equal

to $d_{\text{int}}^{sig} = 0.98$mm while the external diameter d_{ext}^{sig} ranges in $[1.38\ 1.78]$mm. The total diameter of each one of these stranded cables is $d_{\text{cab}}^{\text{sig}} = 18.1$ mm. The difference between the four cables stands in the protection covering the wires. The four samples are surrounded by respectively: an anti-noise tape, a textile sheath, a smooth sheath and a ringed sheath (see Fig. 11).
The sample 5 is made of 5 power wires whose core is made of 105 annealed copper filaments surrounded by an insulating elastomer of cross-linked polyethylene (PE/PP) whose Young's modulus is $E_{\text{PE}} = 1$Gpa and Poisson ration is $\nu_{\text{PE}} = 0.4$. The filaments diameter is $d_{\text{cu}}^{2} = 280\mu$m, the core diameter is $d_{\text{int}}^{pow} = 2.98$mm and the external diameter d_{ext}^{pow} ranges in $[3.62\ 4.50]$mm. Its total diameter is $d_{\text{cab}}^{\text{sig}} = 13$ mm. This sample protection is the same ringed sheath as sample 4.
With all these data, and using the expression (1), the axial Young's modulus for the samples 1 to 4 is in the range $[33.7\ \ 55.4]$ GPa and for the sample 5 is in the range $[49.3\ \ 75.7]$ GPa. Numerically, the axial stiffness being nonessential, the upper bound is arbitrary chosen as nominal value.

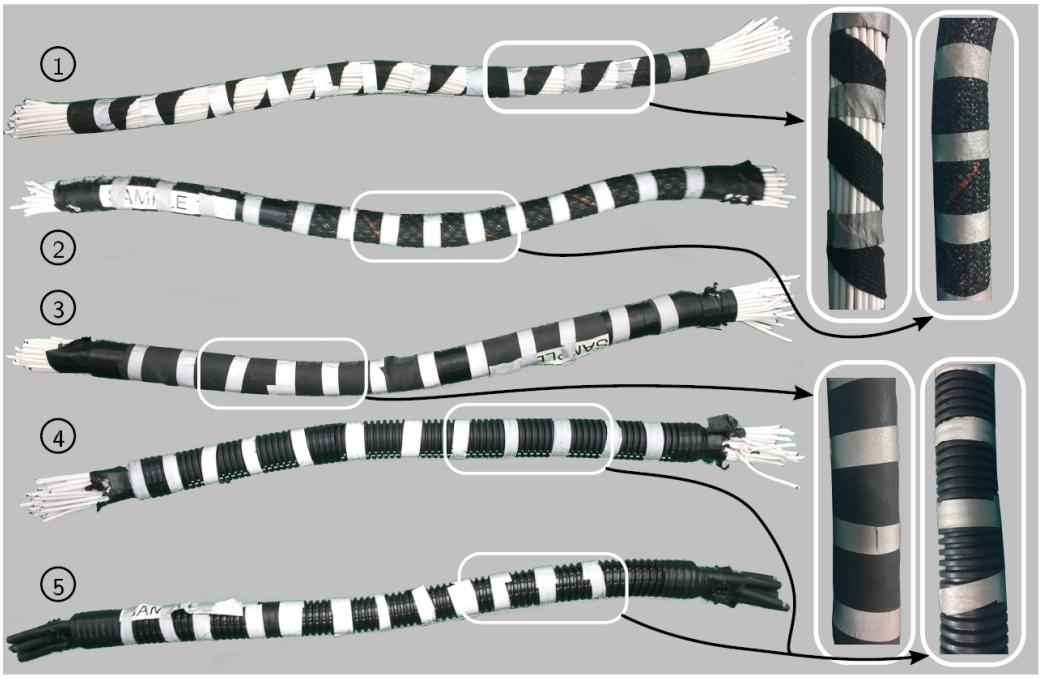

Figure 11: Cables under study numbered from 1 to 5, from top to bottom.

4.2 Test description/measure

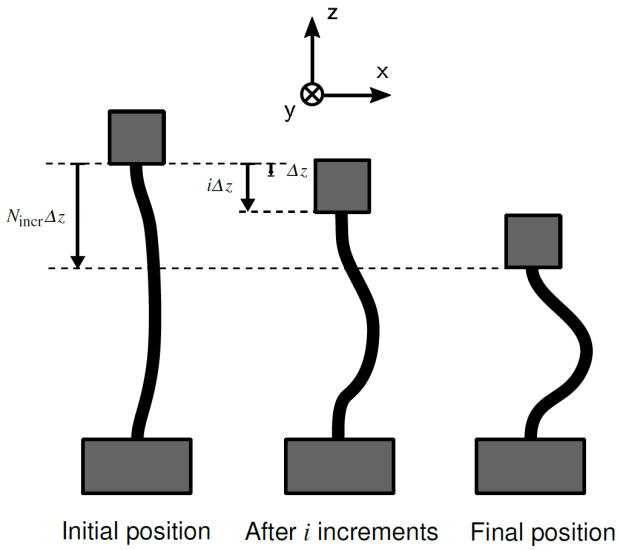

Figure 12: Illustrative scheme of the experimental buckling test seen from camera 1 point of view.

The clamped-clamped buckling test configuration is such as illustrated on figure 12. The loading consists in applying an axial displacement to the top extremity of the cable, achieved in $N_{\text{incr}} = 40$ increments, while the other extremity is clamped. Each one of these increments corresponds to an out-of-charge displacement of norm $\Delta z = 1.75$ mm operated by the robot, so that the total displacement is $N_{\text{incr}}\Delta z = 70$ mm. In practice, as the robot has its own flexibility, it is not the real displacement applied. However, we are able to get the applied force through the force sensor and the displacement applied may be found a posteriori thanks to the vision system. The transverse displacement at the middle of the cable between the initial position and the current position is measured via the vision system. With all these data, the experimental equilibrium curve is obtained (Fig. 13).

4.3 Identification

From the experimental equilibrium curve, the identification process expressed in section 3.4 may be applied. As the 2^{nd} order theory is valid only for moderate rotations, solely the first points of the equilibrium curve are used for identification. An example of identification curve for samples 4 and 5 is presented on figure 13.

The mechanical properties obtained from the identification process explained in section 3 for the EBM and the TM are summarized in table 4. Let us first notice that the range of the identified bending stiffness is very narrow, which is quite reassuring since the cables have all a similar internal structure, except sample 5.
A rough qualitative analysis of the samples protections gives the following expectations for the results:

- the ringed sheath of samples 4 and 5 is only surrounding the cables without sticking to them and as it is smooth does not prevent slipping between the wires;
- the anti-noise tape of sample 1 sticks to the wire but it is not fully covering the sample (gap between the coils) so it weakly blocks the slipping;
- the smooth sheath of sample 3 does not stick to the wires but is not extensible and thus there is a contact interaction between the cable and the protection during bending which makes the cable stiffer in bending direction;
- the textile sheath of sample 2 is very extensible and does not block the slipping between wires.

One would hence expect a low shearing stiffness for samples 1, 2, 4 and 5 and a high shearing stiffness for sample 3. It thus coincides with the results of table 4 except for sample 2 which have a high GA. With respect to the identification results, in the following, we will classify these cables into two categories: low shearing stiffness cables (samples 1, 4 and 5); high stiffness cables (samples 2 and 3).
The values of the experimental maximum initial deflections have also been reported in table 4. They are indeed the only parameters identified that can be compared to measures. There is a quite large discrepancy between the identified deflections and the true initial deflections: for all samples the identified deflection has order of magnitude 1 mm while the real deflection order of magnitude is 10 mm. This discrepancy explains first by the difference between the real initial shape and the model initial shape: the maximum initial deflection does not represent the exact same measure for both cases. It may also simply originate from an error due to the optimization process. Indeed, while not having the same exact contribution (see equation (19)), initial deflection has an effect similar to shearing on the equilibrium curve (see figure 8). As a result, the two parameters

might compensate each other's influence on the actual deflection. In that case, the smaller identified initial deflection would mean that the shearing parameter is underestimated by the optimization process.

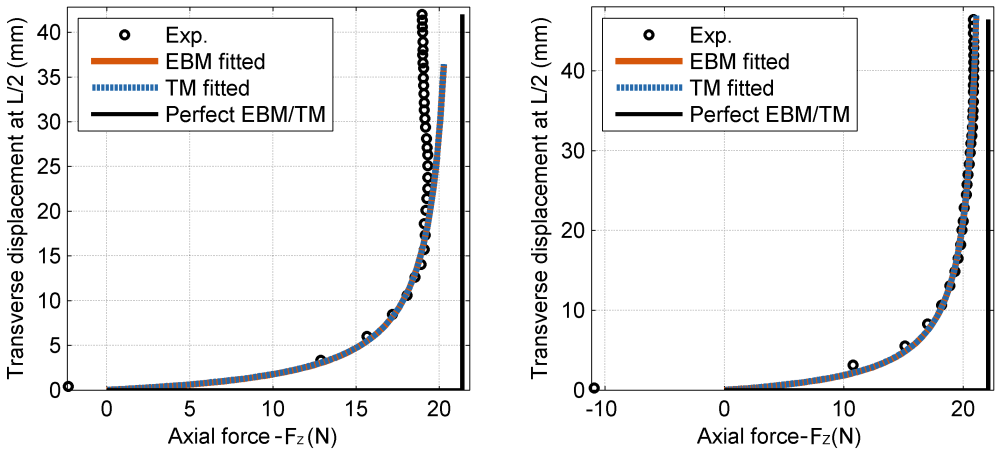

Figure 13: Identification curves on the buckling test for samples 4 and 5.

4.4 Comparison to literature values

It is interesting to compare the results from the identification process with the theoretical results from the literature. According to [Filiatrault and Stearns, 2005], the theoretical bending stiffness ranges in $[EI_{\min}\ EI_{\max}]$. In this range, the minimal bending stiffness $EI_{\min}$ corresponds to all the wires of the cable slipping against each other and thus writes as the sum of the bending stiffness of each wire, that be $EI_{\min} = NE_{\text{comp}}\frac{\pi d_{\text{wire}}^4}{64}$ for N wires of same diameter d_{wire} and Young's modulus E_{comp} obtained from the composite formula (1). The maximal stiffness $EI_{\max}$ corresponds to all the wires sticking against each other and thus forming a unique beam whose stiffness writes $EI_{\max} = E_{\text{comp}}\frac{\pi d_{\text{cab}}^4}{64}$ for a cable of total diameter d_{cab}. With these expressions, the parameters values from section 4.1 and using equation (1) for calculating the Young's modulus E_{cab}, one demonstrated that the ranges are equal to $[3.19\ 80.3]$ Nm^2 for the samples 1 to 4 and $[3.19\ 41.4]$ Nm^2 for the sample 5. The results found in table 4 are far below these ranges. Even if surprising, this result find two explanations. Firstly, there exist uncertainties on the values of the Young's moduli given in section 4.1 which have been obtained from textbooks on the given materials and not by experimental characterization. Secondly,

		Cable	Sample 1	Sample 2	Sample 3	Sample 4	Sample 5
Identified (cf. 3.4)	**Timoshenko**	EI_{T} (mN.m^2)	95.3	64.1	71.9	74.9	79.2
		GA_{T} (N)	43.5	9710	2322	37.8	36.5
		η	$7.38\ 10^{-3}$	$2.08\ 10^{-5}$	$1.04\ 10^{-4}$	$6.67\ 10^{-3}$	$7.31\ 10^{-3}$
		a_0^T (mm)	0.14	0.93	1.2	1.7	1.9
	Euler-Bernoulli	EI_{EB} (mN.m^2)	59.2	63.9	70.9	47.8	49.4
		a_0^{EB} (mm)	0.20	0.93	1.2	2.0	2.2
Eq. (1) | Eq. (2)	**Common parameters**	EA (mN)	14.3	14.3	14.3	14.3	10.0
		GJ (mN.m^2)	1.8	397.6	95.1	1.5	0.77
	True initial deflection	a_0^{exp} (mm)	10.8	9.2	12.2	8.6	10.5

Table 4: Identification results for the 5 samples: values of all the identified or calculated parameters for both the EBM and the TM.

each individual wire of the stranded cables tested is too flexible to be tested on our test bench. As a result, the bending modulus of the wires (which also have a complex internal structure since their core is braided) could not be determined experimentally. As the error on individual wires bending stiffness strongly affects the theoretical range, it is the second main source of error. Let us point out that these conclusions also show that experimental testing is very hard to outmatch by analytical theories for modeling non homogeneous cables.

5 Post-buckling test

5.1 Experimental vs. numerical approach

In the previous sections, the EBM and the TM referred to the 2D buckling theories which were developed for applying the identification process, for understanding the role of shearing in the TM and for comparing both methods. As all these topics have been treated, both these theories are not apropos anymore in the development of this article. For this reason, from this point forward and until further notice, the EBM and the TM will not refer anymore to the buckling theories but in a more general fashion to the 3D nonlinear beam models respectively without shearing and with shearing. In particular, these abbreviations will often refer to the numerical model [Cottanceau et al., 2018] used with or without shearing.
In the coming sections, several experimental results, obtained from the test bench, are compared to numerical results originating from [Cottanceau et al., 2018]. Even though this simulation is based on a geometrically exact beam model, the mechanical parameters found through the identification process described in section 3 (originating from the 2D buckling theory) are used in the simulation, since one assumes they are identical. This simulation is TM-based and takes into account shearing. Nevertheless, as it was shown before, the TM is strictly equivalent to the EBM for $\eta = 0$. For this reason, what is called EBM simulation in the following corresponds to the use of the same numerical tool with the shearing parameter η set to 10^{-8}. Additionally, this numerical simulation takes into account the initial curvature of the cables. As simulations may be run for both the true (real) initial geometry of the cable obtained from the vision system and for an initially perfectly straight (idealized) cable, both cases will be distinguished. The former will be called *real* or *imperfect* cable while the latter will be called *idealized* or *perfect* cable.
As a last warning, to avoid confusions, as numerical and experimental results will be mixed for comparison, it will always be clarified in the main body and the figures which one is discussed, except if it is self-evident.
Finally, let us notice that the following comparisons focus both on the final deformed shapes and on the equilibrium curves during loading. If not explicitly mentioned, the color map on numerical deformed shapes depicts the Von Mises stress on the surface of the cable (computed only for numerical simulations).

5.2 Test description

5.2.1 Experimental

The current section test, denoted post-buckling test, actually corresponds to the continuation of the buckling test. It is therefore exactly such as described in section 4.2 and on figure 12. However, in section 4, solely the first points of the equilibrium curve were exploited for identification and there was no comparisons of the geometries nor of the last points of the equilibrium path.
Let us also notice that, for some of the experimental tests, unloading was also recorded. For these tests, once the $N_{\text{incr}} = 40$ loading increments were achieved, 40 supplementary increments of identical size were applied but in the opposite direction, that being in the z-positive direction.

5.2.2 Numerical

In the numerical simulation, one extremity of the beam is clamped while the other extremity rotations are blocked and its displacements prescribed. As already said in section 4.2, the displacement commanded to the robot corresponds to its out-of-charge displacement and not to the true displacement, since the cable stiffness alters the robot motion. In addition, there might exist a slight bias between the commanded trajectory of the robot (a straight line in the z-axis direction) and the real trajectory (a straight line but not perfectly aligned with the z-axis) due to calibration error. As a result, for a more accurate comparison, the displacement applied in the numerical simulation corresponds to the displacement of the robot tip extracted from the vision system data.
The real simulation is run normally, the initial geometry being extracted from the vision system. For the idealized case, no buckling direction is favored, and the cable could possibly buckle in any direction. For this reason, an initial deflection similar to the one of the analytical model (section 3, of the form $w_0(x) = \frac{a_0}{2}\left(1-\cos\left(\frac{2\pi x}{L}\right)\right)$) was added. As this perturbation is purely artificial and determines the buckling direction, it is not relevant to compare the geometry of the idealized case to the experimental geometry. The idealized case is thus restricted to the equilibrium curves comparison.

5.3 Results

The equilibrium curves of samples 2 and 4 for the post-buckling test are depicted respectively on figures 14 and 15. The corresponding deformed shapes in initial

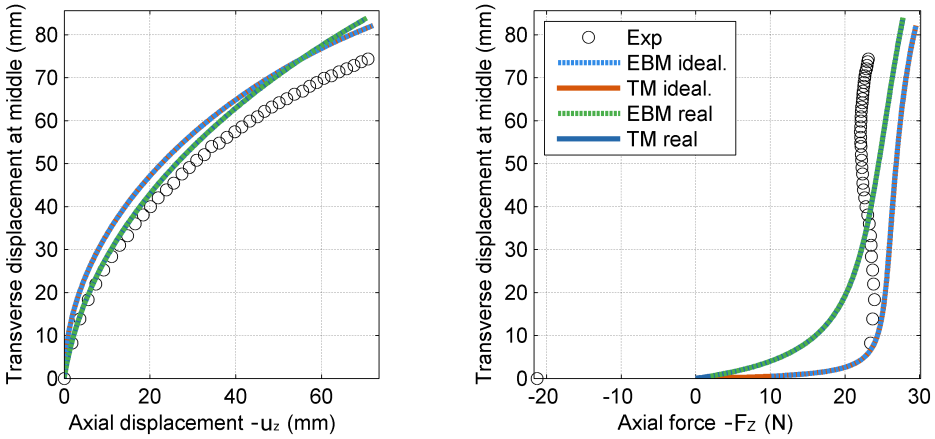

Figure 14: Post-buckling test - Equilibrium curves for sample 2 (large identified *GA*): transverse displacement of the beam middle vs. axial displacement (left) and axial force (right).

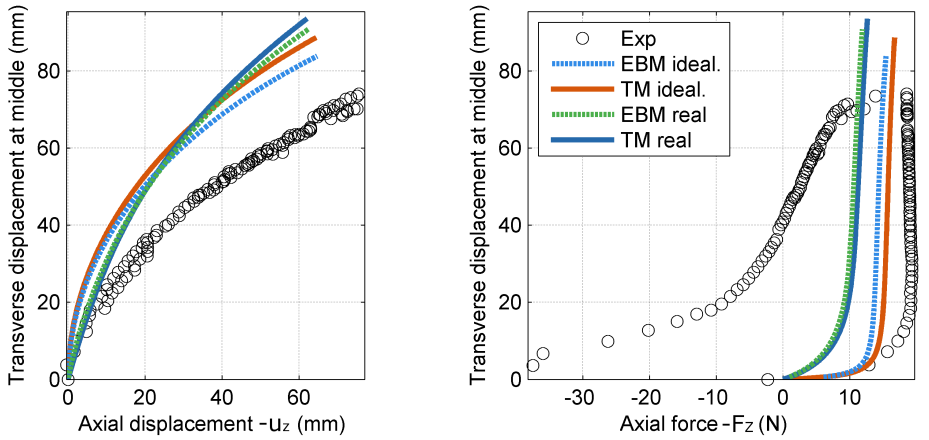

Figure 15: Post-buckling test - Equilibrium curves for sample 4 (small identified *GA*): transverse displacement of the beam middle vs. axial displacement (left) and axial force (right).

and final configurations are pictured on figures 16 and 17. Samples 2 and 4 were chosen as illustration here because the sample 2 is representative of the samples with a large identified *GA* while the sample 4 represents the samples with a small identified *GA* (see section 4.3).

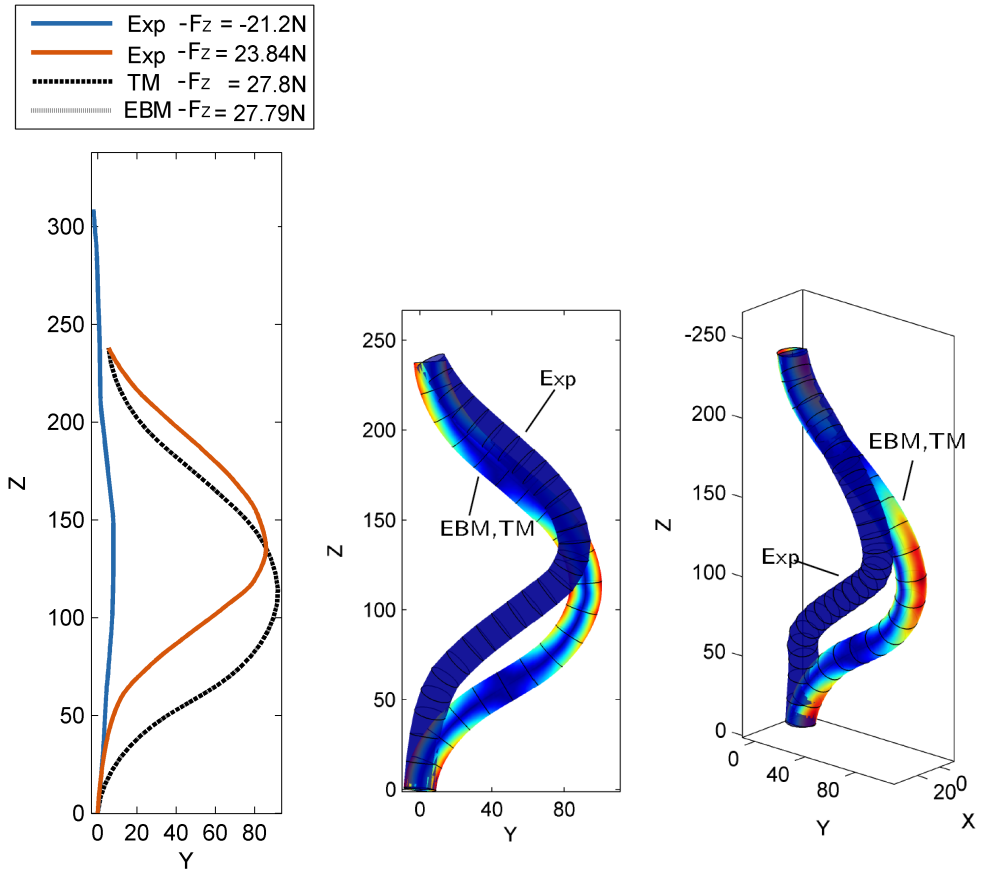

Figure 16: Post-buckling test - Final deformed shape of sample 2 with TM, EBM vs. experimental deformed shape.

Observing the force-based equilibrium curves, the reader will notice that the numerical model (for both EBM and TM) do not superimpose well with the experimental points even for the idealized model, especially for sample 4. It may look erroneous but, as explained in section 5.2.2, the numerically applied displacement is not solely an axial displacement but the displacement extracted from the vision system, which may have small components in x and y direction as well but is a more objective measure of the real loading. It is thus common sense that the curve does not match perfectly the idealized analytical curve which was used for identification.

This difference aside, the first comment one can made on equilibrium curves is that while the numerical curves have qualitatively the same form as the experimen-

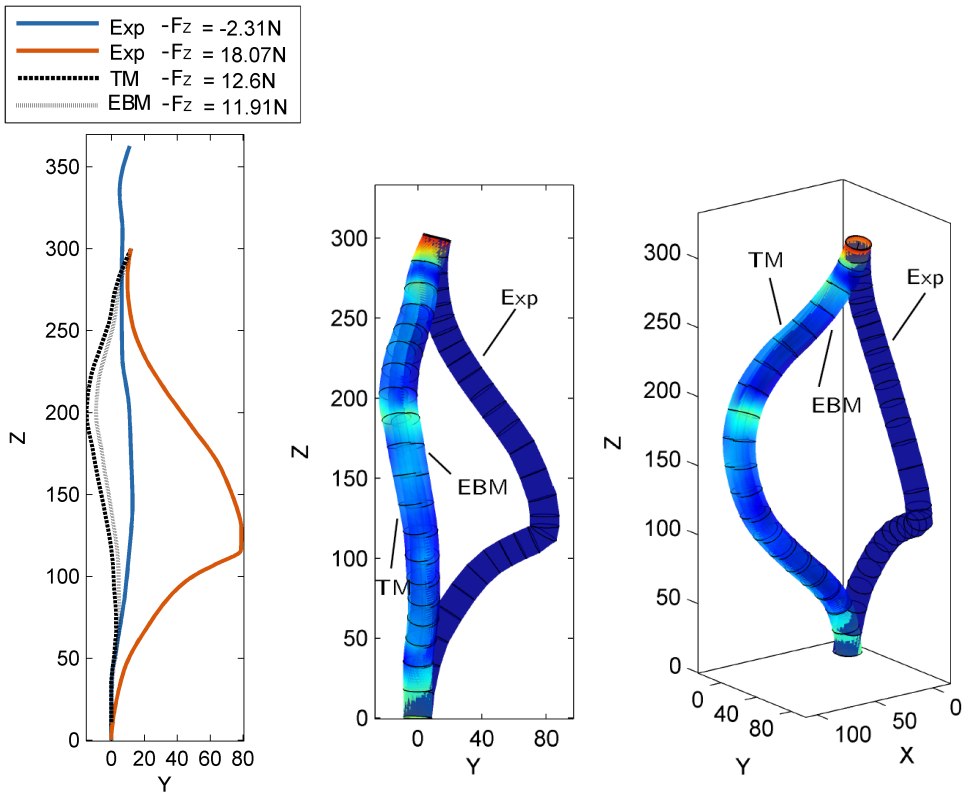

Figure 17: Post-buckling test - Final deformed shape of sample 4 with TM, EBM vs. experimental deformed shape.

tal curves, the values are different. For displacement-based curves, the transverse displacement is always greater on numerical simulations. The more likely explanations are the unexpected local and sometimes abrupt changes of curvature due to local phenomena observed on the deformed shapes (see Fig.16 and 17). These local phenomena may appear because the cable is not totally homogeneous along its centerline and local weaknesses appear. The non-homogeneity is caused by unconventional arrangements of the wires and the interaction between the wires and the protection. For the force-based equilibrium curves, even if the order of magnitude is acceptable, there exists a significant difference between the real simulation and the experimental points. This difference comes from a flaw which is greater in the real cable than the flaw a_0 of the analytical model obtained by the optimization process: this initial curvature plays a softening role, as justified in section 3.3, and explains why the reaction force is systematically underestimated in the real

simulation.
Besides, one notices that equilibrium paths are very similar for both the EBM and the TM whether displacement-based or force-based curve and whether idealized or real model are looked at. For the large *GA* case (sample 2), the EBM and the TM even coincide almost perfectly and illustrate the fact that the EBM is the limit case of the TM when *GA* tends to infinity. When *GA* is smaller, the transverse displacement is slightly greater for the TM because the shearing makes the cable more flexible but stay very close to the EBM.
Finally, in both models, it looks like accounting for initial curvature does not improve the results on this example and that the buckling direction prediction is not very robust (looks well for the sample 2 and not well for the 4) as proved by displacement-based paths and deformed shapes. However, as a buckling test is very sensitive to any perturbation, these errors may be easily understood .
As a last and purely experimental remark, the experimental force-based curve of figure 15 which contains the unloading step reveals an hysteresis: the reaction force is smaller on the way back. It is clearly explained by dry friction as explained in introduction of this paper.

6 3D displacement

The procedure for this test is exactly the same as the procedure described in section 5.1 for the post-buckling test and is not recalled here.

6.1 Test description

Experimentally, the 3D displacement test configuration is such as illustrated on figure 18. The loading consists in applying a 3D displacement (not only in axial direction) to the top extremity of the cable, achieved in $N_{\text{incr}} = 36$ increments, while locking its rotational degrees of freedom and with the bottom extremity clamped. Each one of these increments corresponds to an out-of-charge displacement $\Delta\boldsymbol{u} = [\Delta x \;\; \Delta y \;\; \Delta z]^T$ with $\Delta x = -4$ mm, $\Delta y = 0.5$mm and $\Delta z = -3$ mm.
Numerically, the simulation is set up following the exact same procedure as in section 5.2.2, except for the initial geometry of the idealized case which is here perfectly straight (unlike buckling test, there is no need of initial perturbation).

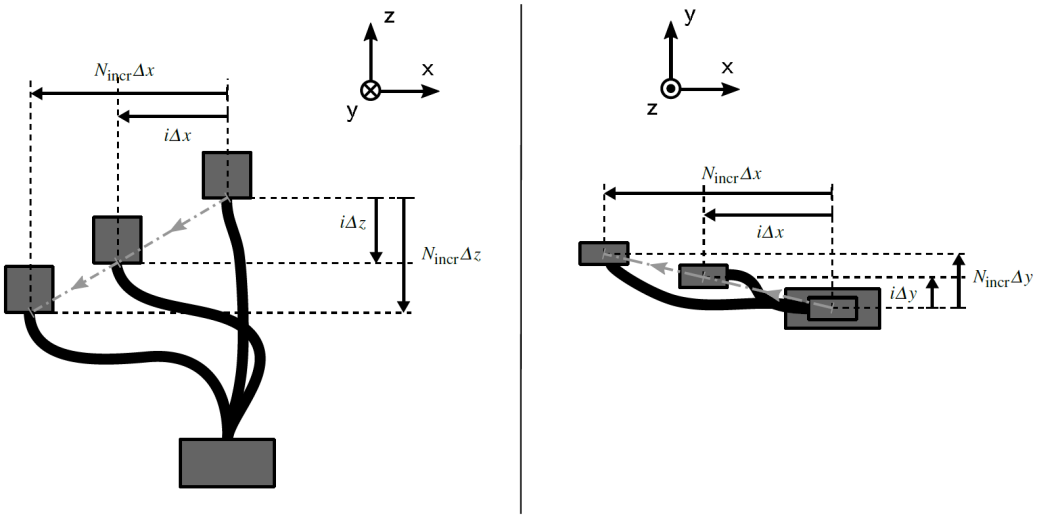

Figure 18: 3D displacement test illustrative scheme seen from camera 1's point of view (left) and from above (right).

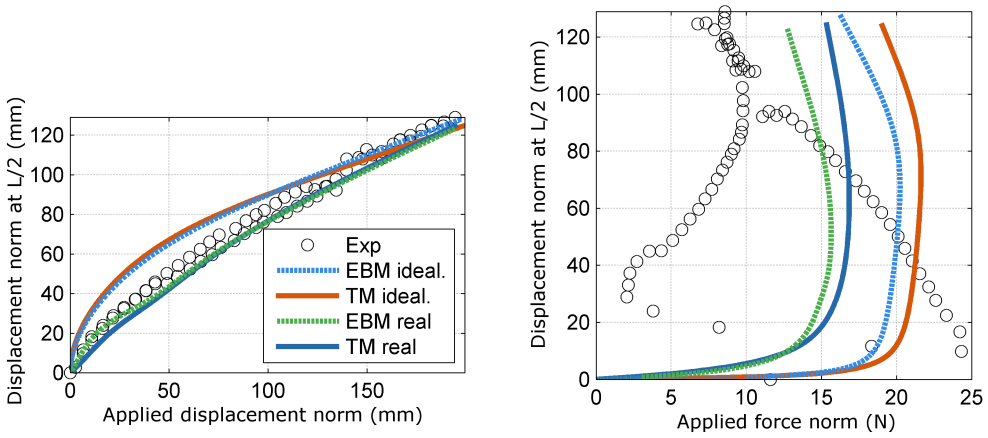

Figure 19: 3D displacement test - Equilibrium curves for sample 1: transverse displacement at beam middle vs. axial displacement (left) and axial force (right).

6.2 Results

The equilibrium curves of samples 1 and 3 for the 3D displacement test are depicted respectively on figures 19 and 20. The corresponding deformed shapes in the final configuration are pictured on figures 22 and 23. The evolution of the

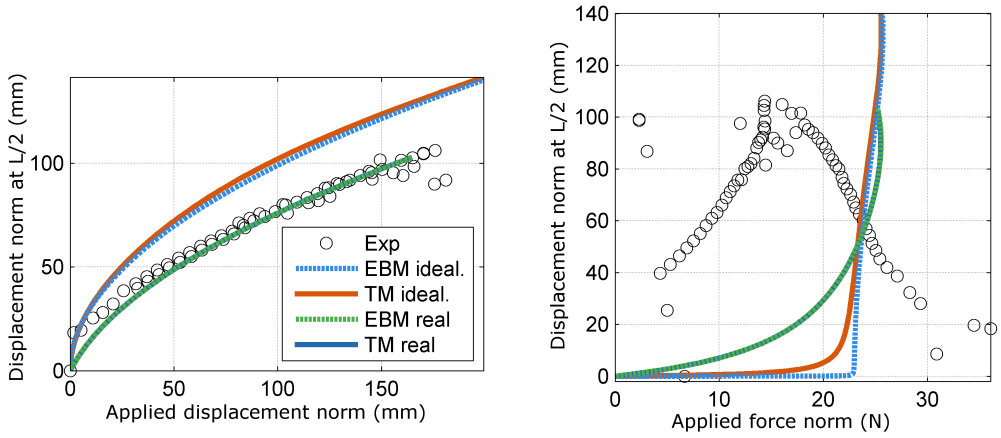

Figure 20: 3D displacement test - Equilibrium curves for sample 3: transverse displacement at beam middle vs. axial displacement (left) and axial force (right).

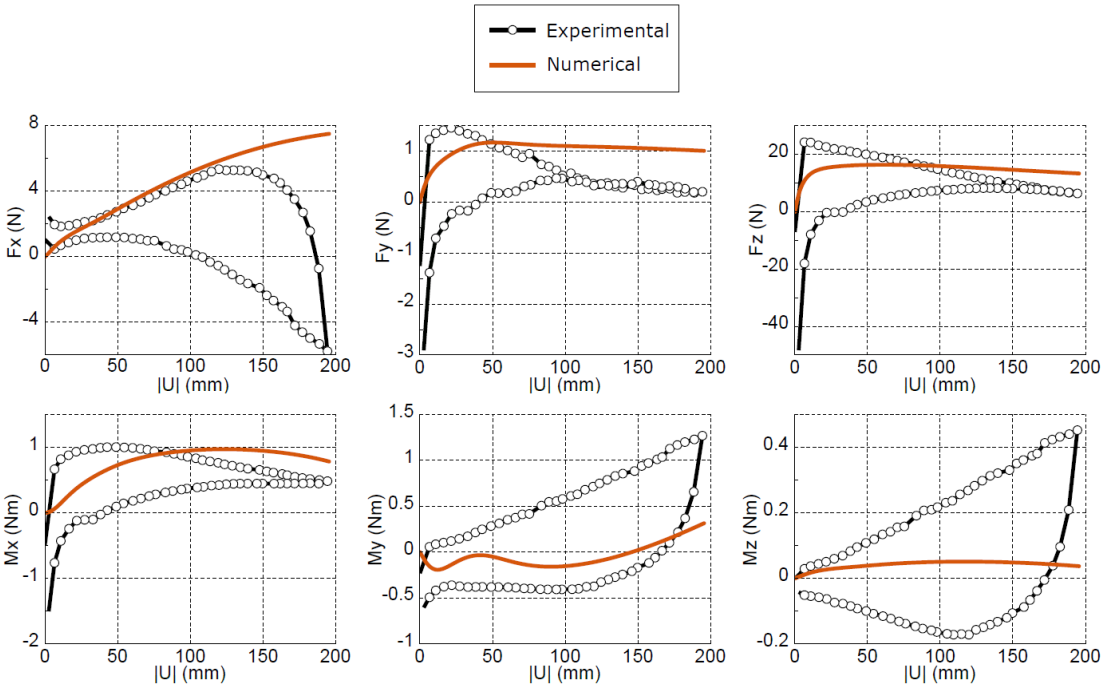

Figure 21: 6 reaction forces and torques during loading for the experiment and the real Timoshenko model - sample 1.

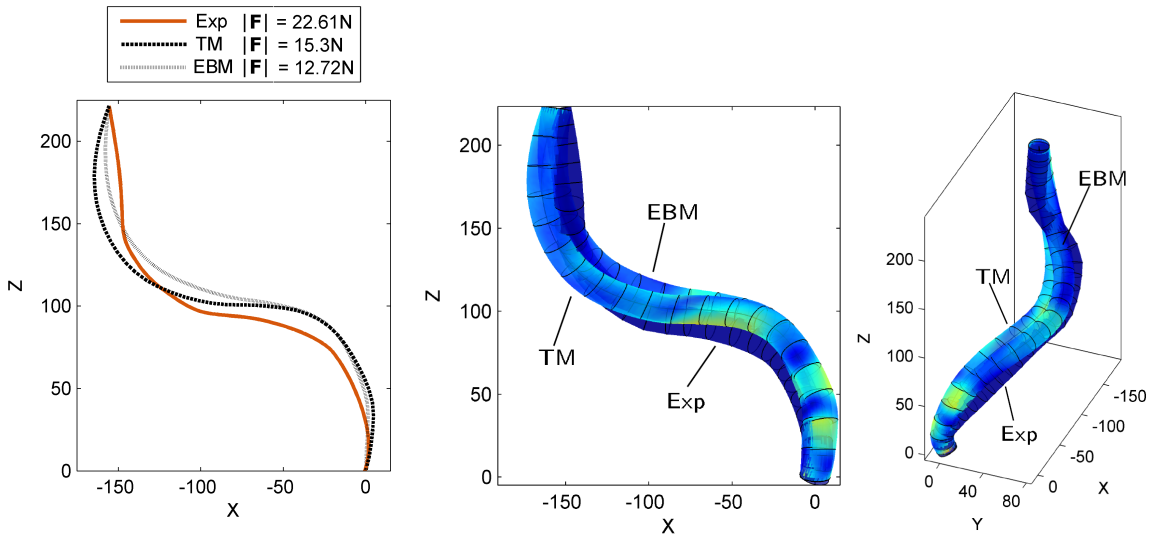

Figure 22: 3D displacement test - Final deformed shapes of sample 1 with TM, EBM vs. experimental deformed shape.

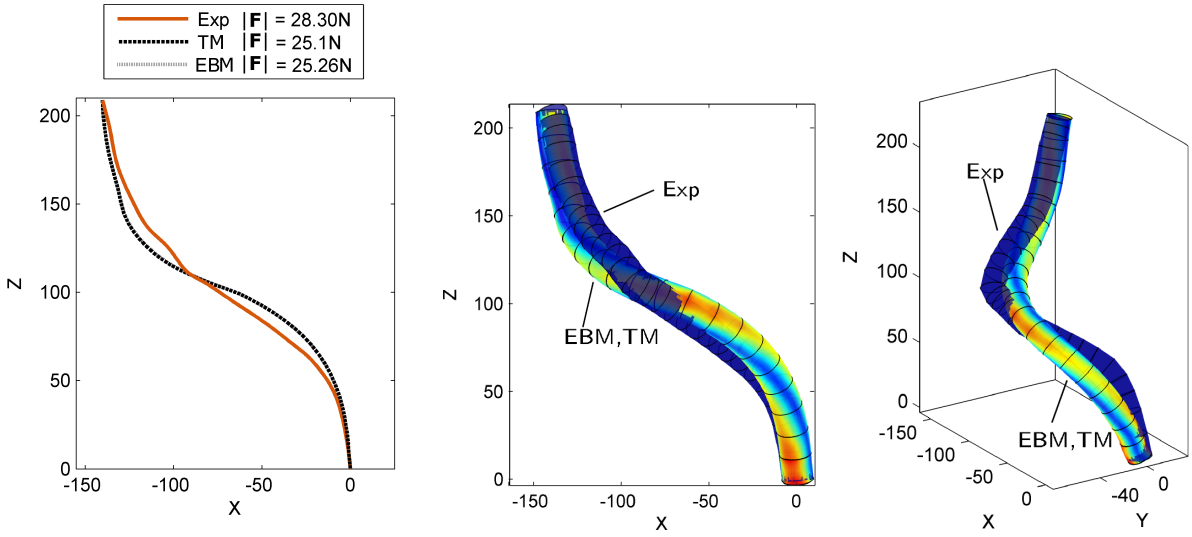

Figure 23: 3D displacement test - Final deformed shapes of sample 3 with TM, EBM vs. experimental deformed shape.

reaction forces and torques along loading are also provided for sample 1 in figure 21.

The numerical force-based equilibrium curves are quite different from the experimental ones, even the equilibrium path shape being unalike. Despite that, the order of magnitude predicted, which is what really matters in an industrial environment, is fairly good for all samples. In addition, the evolution of the reaction force components shows that the numerical model predicts well the main contribution of forces in x and z directions, even if the values are different. As for the post-buckling test, the reaction force of the real beam is lesser than the idealized beam on the equilibrium curve in this example because of the bigger initial flaw. These results are confirmed by the evolution of the forces components.

The displacement-based paths evidence a very good prediction of the geometry by the numerical model, confirmed by the deformed shapes: the numerical shapes differ only from the experimental shapes because they are smoother (no local changes of curvature). Accounting for the initial curvature in this example leads to a great improvement of the geometry and the displacement-based curves in this configuration almost match perfectly the experimental ones which is really noteworthy.

As for the post-buckling test of section 5, the difference between the EBM and the TM on the geometry is very subtle, even for the small *GA* case (sample 1, Fig. 22). The difference is more noticeable for the reaction forces of sample 1 but stay very alike for both models.

Finally, the experimental force vs. displacement curves evidence again a different path between loading and unloading, justified by dry friction. Additionally, one observes even during loading a large force drop which was also noticeable on the post-buckling test for sample 2 in a less significant manner (Fig. 14). This phenomenon is probably due to a relaxation process at the boundary conditions. The struggle to apply a strict clamping to a structure is indeed a well known problem [Ritto et al., 2008] which we choose to put aside in this paper but which necessarily alters the results on force reaction.

7 Influence of uncertainties on deformed shapes

In this section, the 3D displacement test described in section 6.1 is again studied but only numerically. Hereinafter, influence of uncertainties on the identified parameters and on the initial geometry for the TM, which are the main inputs of the simulation, is observed.

7.1 Influence of shearing stiffness identification

7.1.1 Test description

This section focuses on the validity of the shearing stiffness identification and its role on the final deformed shape. In this first uncertainties study, the axial stiffness EA and the bending stiffness EI are kept constant and equal to their nominal value identified in section 4.3. If we denote GA_{id} the value of shearing stiffness identified in section 4.3, the shearing stiffness is herein taken into the range $[0.1GA_{\text{id}}\ , 10GA_{\text{id}}]$. Since the torsional stiffness chosen for the simulation depends on the identified GA, one study two cases here:

- a case in which GJ is kept constant and equal to its identified nominal value;
- a case in which it is calculated from the shearing stiffness with the formula (2).

This allows to assess the choice we have made to determine GJ without devising another test.
Then, the numerical simulation is run for the two cases, for 50 values of GA linearly chosen on a logarithmic scale of the range mentioned above. All the final geometries are then gathered and a surface surrounding these geometries is generated, which corresponds to the volume swept by the cable for the varying GA.

7.1.2 Results

The results of this test for the samples 1 and 3 are displayed on figures 24 and 25. These figures have several common features which leads to several significant results:

- The volume covered is very wide, which demonstrates the importance of well chosen parameters. In particular, for the sample 1, there exists two main types of deformed shape: either the cable bends in the Y-positive direction either it bends in the Y-negative direction. A bad identification may thus lead to very erroneous solution.
- The volume covered is quite wide for both cases but there are not any improvements on the geometries predicted (see figures 22 and 23): it thus strengthens the choice of the method of identification described in section

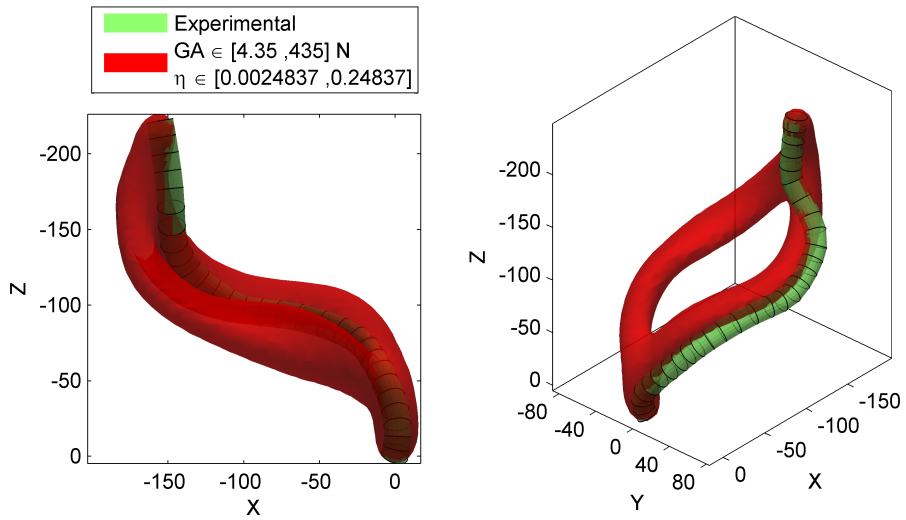

(a) Varying GJ.

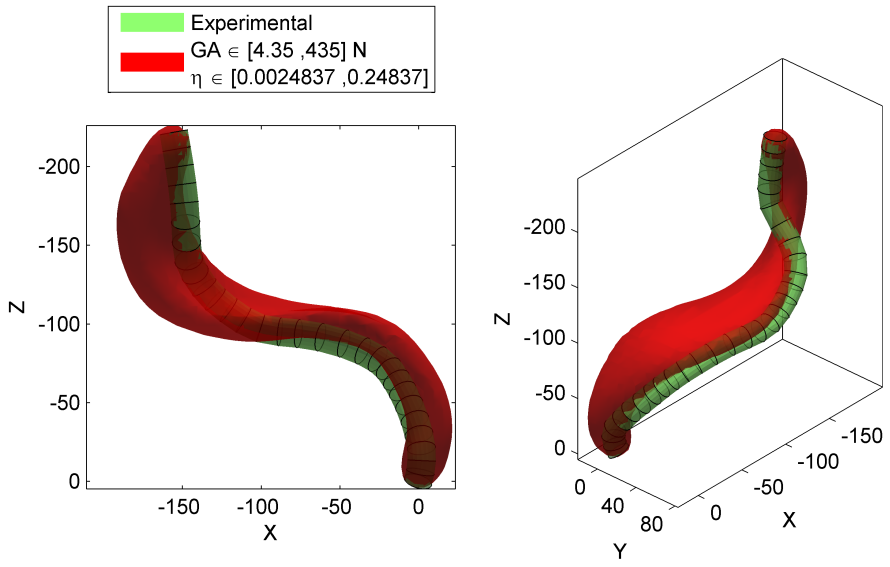

(b) Fixed GJ.

Figure 24: Volume swept by the cable in the final configuration for a varying GA - sample 1.

3.4. In particular, the venture of calculating GJ from GA as for a homogeneous beam seems to give good results. Let us denote that although the experimental cable is not contained in this volume, it is mainly due to imprecision on the length of the cable and not on the identified parameters.

- Both cases, especially the sample 3, evidence the paramount importance of the torsional stiffness. For the sample 3, the geometry almost does not change at all when GJ does not vary while it changes a lot in the second case. GJ looks much more important than GA on the predicted deformed shape. For the sample 1, it is less obvious but when GJ is kept constant the volume covered is smaller and only one of the two branches (the good one) cited above persists, which confirms this result: GA needs to be well identified but have a limited impact on the geometry compared to GJ.

7.2 Influence of bending stiffness identification

7.2.1 Test description

This section focuses on the validity of the bending stiffness identification and its role on the final deformed shape. In this second uncertainties study, the axial stiffness EA, the torsional stiffness GJ and the shearing stiffness GA are kept constant and equal to their nominal value identified in section 4.3. If we denote EI_{id} the value of bending stiffness identified in section 4.3, the bending stiffness is herein taken into the range $[0.1EI_{\text{id}}\ , 10EI_{\text{id}}]$. For 50 values of EI linearly chosen on a logarithmic scale of the range mentioned above, the numerical simulation is run. All the final geometries are then gathered and a surface surrounding these geometries is generated, which corresponds to the volume swept by the cable for varying EI.

7.2.2 Results

The outcomes of this test for the samples 1 and 3 are displayed on figures 26 and 27. The first striking observation originating from these curves is that the volume swept is almost identical to the volume swept for the first case of section 7.1 (figures 24(a) and 25(a)). The torsional stiffness and the flexural stiffness have the same effect on the geometry.
Besides, in both experiments, the ratio of flexural over torsional stiffness belongs

to the same range :

$$\frac{EI}{GJ} \in \left[0.1,\ \ 10\right] \cdot \frac{EI_{\text{id}}}{GA_{\text{id}}} \frac{J_{\max}}{A_{\max}}. \tag{21}$$

As a result, a possible explanation to the almost identical results is the very influential role of the ratio $\frac{EI}{GJ}$ on the final geometry. The study of this factor is out of the scope of this article.
As a consequence of the similarity between section 7.1 and the present results, the conclusions are the same. In particular, our identification process seems to give good results since the geometry is not improved by varying EI.

7.3 Influence of the initial geometry

7.3.1 Test description

This section focuses on the role played by the initial geometry on the final deformed shape. For that, a random initial configuration was generated by creating 10 equally-spaced points along the z-direction. The transverse coordinates of the 8 interior points were chosen according to a uniform law for x and y on the respective ranges $[-X_0^{\max},\ X_0^{\max}]$ and $[-Y_0^{\max},\ Y_0^{\max}]$, with $X_0^{\max}$ and $Y_0^{\max}$ the maximal values of the coordinates in x and y directions of the real cable in its initial configuration: the points are thus contained in the right prism surrounding the real cable. The first and the last of these 10 points were chosen such that their position coincides with the extremities of the real cable. The 10 points are then interpolated by a 3D spline to form the initial centerline. For each of the 50 random initial geometry, the simulation is then run and the final deformed shape obtained. All the final geometries are then gathered and a surface surrounding these geometries is generated, which corresponds to the volume swept by the cable for the varying initial geometry.

7.3.2 Results

The results of this test for the samples 1 and 3 are displayed on figures 28 and 29. They clearly demonstrate two main results. Firstly, the volume covered by the final shapes is very large in comparison to the initial volume: for the sample 1, it is around 4.5 times superior to the initial volume and for the sample 2 it is 2.35 times superior. It hence shows that a small change in the the initial configuration may lead to a large change in the final deformed shape and that initial geometry plays a very important role on the final geometry.

Besides, in spite of the large volume covered, the experimental deformed shape is not contained in the volume predicted for both cases. It is noticeable in a moderate way for sample 1 which is on the border of the volume but very noteworthy for sample 3 for which the experimental geometry is clearly outside. When one compares this result to the very good prediction observed on figure 23, it appears very influential: it means that making one simulation is the good initial geometry is better than a large number of simulations using a randomly generated initial geometry. Consequently, it proves that not taking into account initial curvature may lead to a considerable imprecision on the results.

8 Conclusion

In this paper, an experimental method for the validation of a numerical 3D geometrically exact beam model for the simulation of cables assembly has been presented. As part of this method, a test bench allowing a quasi-static study of the cables behavior has been devised. This bench allows to apply 3D displacements and rotations to one end of the cable while the other end is clamped. The reaction force and the centerline position are extracted thanks to respectively a force sensor and a vision system. Taking advantage of the bench versatility, a buckling test has been set up and, with the help of the buckling theory, is used for identification of the homogeneous beam shearing parameter GA and bending stiffness EI of 5 samples of cables. The axial stiffness EA, which has less importance in the industrial field of use, is reckoned from the geometrical and material properties of the cable. The torsional stiffness GJ is retrieved from the identified GA and geometrical properties. This identification features only one test for the determination of the mechanical parameters and avoids devising another setup.
Using these identified parameters as inputs of the numerical model, two other experiments are confronted with the simulation: a post-buckling study and a 3D displacement test. The comparison is carried out on the deformed shape and on the equilibrium curve. Lastly, a numerical study is carried out focusing on the uncertainties of the parameter identification and of the initial geometry and their impact on the final geometry.
Gathering the results of all these studies, which reveal several common features, allows to draw the following conclusions:

- The Timoshenko model and the Euler-Bernoulli model give very similar results even for a beam with low shearing stiffness. This conclusion stands

for both the deformed shape and the reaction force prediction. As a result, the shearing has a very small role for modeling the quasi-static behavior of stranded cables, which is confirmed by the uncertainties study.

- The torsional stiffness GJ plays an important role on the final geometry. As a proof, the uncertainties study of section 7 shows that a large variability in the final shape is observed when GJ varies. Furthermore, the ratio $\frac{EI}{GJ}$ looks like a very influential mechanical parameter for the final geometry (see the common results of sections 7.1 and 7.2).

- The buckling test seems as a good way to identify beam parameters since only one test is necessary. In particular, the determination of GJ from GA value gives very good results. It is confirmed by the fact that the geometry is not improved by taking GJ values in a wide range surrounding the value identified.

- The beam model used with the identification presented with this article gives:

  - Excellent results for the final geometry. It is amazingly good for the 3D displacement test, apart from a few local changes of curvatures which do not spoil the final geometry. It looks less true for the post-buckling example but it is a very demanding test. There indeed exists a wide range of buckling directions possible for a loading case which does not favor any deformation direction. In this case, the internal structure, local phenomena or simply the error of measure of the initial deformed shape are perturbations that may explain the bad prediction. However, in an industrial environment, such a demanding case is pretty rare, and this conclusion should not question the good results obtained for the 3D displacement.
  - Only average results for the reaction forces likely because of dry friction. Nevertheless, let us notice that the order of magnitude is correct and that the dominating force components are well predicted, which is a fair point for automotive industry purposes.
  - The two points above are true for the 5 samples tested. It thus seems that despite their variety, the model works identically for any protection used.

- The initial geometry which was accounted for in the numerical model is also of paramount importance for the final shape prediction. It seems that not considering it may lead to very erroneous results.
- The values of bending stiffness obtained from the identification are not even contained in the classical range of values of the literature. It thus seems that analytically homogenized values may give wrong results.

To support these conclusions, additional experimental tests focusing on the quasi-static manipulation of stranded cables in the 3D space should be carried out. Indeed, the lack of a wide literature on this topic prevents from generalizing these results to all sorts of stranded cables. In addition, an analytical study of the ratio $\frac{EI}{GJ}$ influence on the geometry seems as an interesting sequel to this work, as it looks preponderant in the model. Besides, dry friction is clearly present in this type of structures. Future researches on a way to account for the dry friction effect in the beam model without spoiling its benefits (few parameters to identify, small number of degrees of freedom) are also of great concerns. Likewise, pre-strains have been studied in this paper but a thorough study of pre-stresses is of interest.

Acknowledgments

The authors thank Renault Group for the provision of the cable samples. The authors would also like to acknowledge Jean-Paul Decocq, Adel Olabi, François-Xavier Vérin, Gil Boyé de Sousa and Franck Hernoux for their help and support to devise and set up the test bench.

References

[Ope, 1999] (1999). OpenCV user site.

[Ardelean et al., 2014] Ardelean, E. V., Babuška, V., Goodding, J. C., Coombs, D. M., Robertson III, L. M., and Lane, S. A. (2014). Cable effects study: tangents, rabbit holes, dead ends, and valuable results. *Journal of Spacecraft and Rockets*.

[Bažant and Cedolin, 2010] Bažant, Z. and Cedolin, L. (2010). *Stability of Structures: Elastic, Inelastic, Fracture and Damage Theories*. World Scientific.

[Bertails et al., 2006] Bertails, F., Audoly, B., Cani, M.-P., Querleux, B., Leroy, F., and Lévêque, J.-L. (2006). Super-helices for predicting the dynamics of natural hair. In *ACM Transactions on Graphics (TOG)*, volume 25, pages 1180–1187. ACM.

[Cardou and Jolicoeur, 1997] Cardou, A. and Jolicoeur, C. (1997). Mechanical models of helical strands. *Applied Mechanics Reviews*, 50:1–14.

[Castello and Matt, 2011] Castello, D. A. and Matt, C. F. T. (2011). A validation metrics based model calibration applied on stranded cables. *Journal of the Brazilian Society of Mechanical Sciences and Engineering*, 33(4):417–427.

[Chen et al., 2015] Chen, Z., Yu, Y., Wang, X., Wu, X., and Liu, H. (2015). Experimental research on bending performance of structural cable. *Construction and Building Materials*, 96:279–288.

[Coleman and Li, 1996a] Coleman, T. F. and Li, Y. (1996a). An interior trust region approach for nonlinear minimization subject to bounds. *SIAM Journal on optimization*, 6(2):418–445.

[Coleman and Li, 1996b] Coleman, T. F. and Li, Y. (1996b). A reflective newton method for minimizing a quadratic function subject to bounds on some of the variables. *SIAM Journal on Optimization*, 6(4):1040–1058.

[Coombs et al., 2011] Coombs, D. M., Goodding, J. C., Babuska, V., Ardelean, E. V., Robertson, L. M., and Lane, S. A. (2011). Dynamic modeling and experimental validation of a cable-loaded panel. *Journal of Spacecraft and Rockets*, 48(6):958–973.

[Cottanceau et al., 2018] Cottanceau, E., Thomas, O., Véron, P., Alochet, M., and Deligny, R. (2018). A finite element/quaternion/asymptotic numerical method for the 3d simulation of flexible cables. *Finite Elements in Analysis and Design*, 139:14–34.

[Filiatrault and Stearns, 2005] Filiatrault, A. and Stearns, C. (2005). Flexural properties of flexible conductors interconnecting electrical substation equipment. *Journal of Structural Engineering*, 131(1):151–159.

[Goodding et al., 2011] Goodding, J. C., Ardelean, E. V., Babuška, V., Robertson III, L. M., and Lane, S. A. (2011). Experimental techniques and structural

parameter estimation studies of spacecraft cables. *Journal of Spacecraft and Rockets*, 48(6):942–957.

[Goodding et al., 2008] Goodding, J. C., Griffee, J. C., and Ardelean, E. V. (2008). Parameter estimation and structural dynamic modeling of electrical cable harnesses on precision structures. In *49th AIAA/American Society of Mechanical Engineers/American Society of Civil Engineers/American Helicopter Society/Adaptive Structures Conference Structures, Structural Dynamics, and Materials Conference*, pages 2008–1852.

[Hill, 1964] Hill, R. (1964). Theory of mechanical properties of fibre-strengthened materials: I. Elastic behaviour. *Journal of the Mechanics and Physics of Solids*, 12(4):199–212.

[Huang, 1978] Huang, N. (1978). Finite extension of an elastic strand with a central core. *ASME J. Appl. Mech*, 45(4):852–858.

[Irschik and Gerstmayr, 2011] Irschik, H. and Gerstmayr, J. (2011). A continuum-mechanics interpretation of reissner's non-linear shear-deformable beam theory. *Mathematical and Computer Modelling of Dynamical Systems*, 17(1):19–29.

[Jolicoeur and Cardou, 1996] Jolicoeur, C. and Cardou, A. (1996). Semicontinuous mathematical model for bending of multilayered wire strands. *Journal of engineering Mechanics*, 122(7):643–650.

[LeClair and Costello, 1988] LeClair, R. and Costello, G. (1988). Axial, bending and torsional loading of a strand with friction. *Journal of Offshore Mechanics and Arctic Engineering*, 110(1):38–42.

[Linn et al., 2008] Linn, J., Stephan, T., Carlsson, J., and Bohlin, R. (2008). Fast simulation of quasistatic rod deformations for vr applications. In *Progress in Industrial Mathematics at ECMI 2006*, pages 247–253. Springer.

[Love, 1944] Love, A. (1944). A treatise on the mathematical theory of elasticity.

[Papacharalampopoulos et al., 2016] Papacharalampopoulos, A., Makris, S., Bitzios, A., and Chryssolouris, G. (2016). Prediction of cabling shape during robotic manipulation. *The International Journal of Advanced Manufacturing Technology*, 82(1-4):123–132.

[Papailiou, 1997] Papailiou, K. (1997). On the bending stiffness of transmission line conductors. *IEEE Transactions on Power Delivery*, 12(4):1576–1588.

[Raoof and Hobbs, 1988] Raoof, M. and Hobbs, R. E. (1988). Analysis of multilayered structural strands. *Journal of engineering Mechanics*, 114(7):1166–1182.

[Reissner, 1981] Reissner, E. (1981). On finite deformations of space-curved beams. *Zeitschrift für angewandte Mathematik und Physik ZAMP*, 32(6):734–744.

[Ritto et al., 2008] Ritto, T. G., Sampaio, R., and Cataldo, E. (2008). Timoshenko beam with uncertainty on the boundary conditions. *Journal of the Brazilian Society of Mechanical Sciences and Engineering*, 30(4):295–303.

[Sathikh et al., 1996] Sathikh, S., Moorthy, M., and Krishnan, M. (1996). A symmetric linear elastic model for helical wire strands under axisymmetric loads. *The Journal of Strain Analysis for Engineering Design*, 31(5):389–399.

[Sendeckyj, 2016] Sendeckyj, G. (2016). Elastic behavior of composites. *Composite Materials*, 2:45–83.

[Simo and Vu-Quoc, 1986] Simo, J. C. and Vu-Quoc, L. (1986). A three-dimensional finite-strain rod model. part ii: Computational aspects. *Computer methods in applied mechanics and engineering*, 58(1):79–116.

[Spak et al., 2013] Spak, K., Agnes, G., and Inman, D. (2013). Cable modeling and internal damping developments. *Applied Mechanics Reviews*, 65(1):010801.

[Spak et al., 2014] Spak, K., Agnes, G., and Inman, D. (2014). Parameters for modeling stranded cables as structural beams. *Experimental Mechanics*, 54(9):1613–1626.

[Utting and Jones, 1987a] Utting, W. and Jones, N. (1987a). The response of wire rope strands to axial tensile loads—part i. experimental results and theoretical predictions. *International journal of mechanical sciences*, 29(9):605–619.

[Utting and Jones, 1987b] Utting, W. and Jones, N. (1987b). The response of wire rope strands to axial tensile loads—part ii. comparison of experimental results and theoretical predictions. *International journal of mechanical sciences*, 29(9):621–636.

[Yu, 1949] Yu, A.-T. (1949). *Vibration damping of stranded cable*. PhD thesis, Lehigh University.

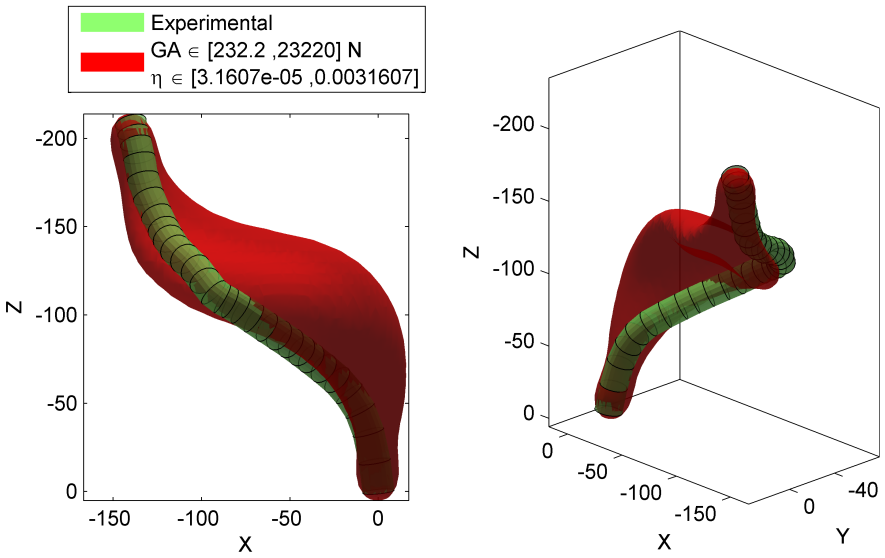

(a) Varying *GJ*.

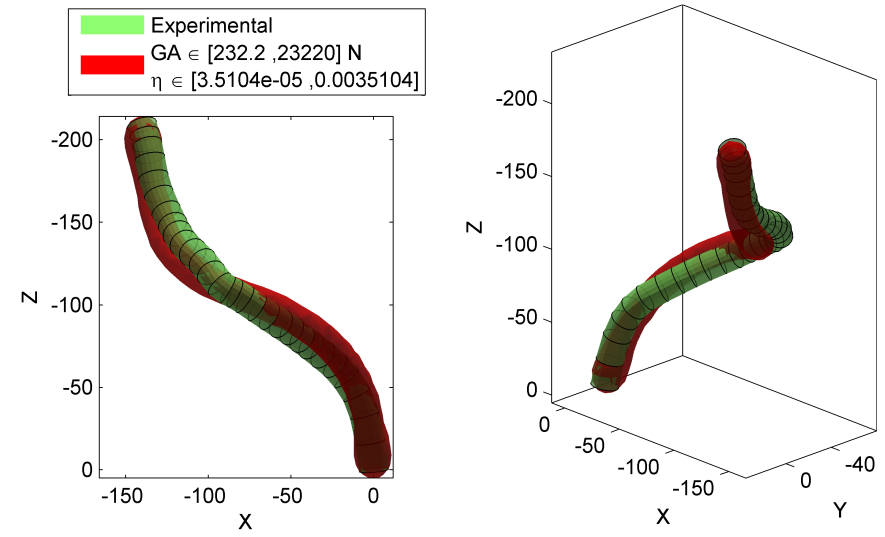

(b) Fixed *GJ*.

Figure 25: Volume swept by the cable in the final configuration for a varying *GA* - sample 3.

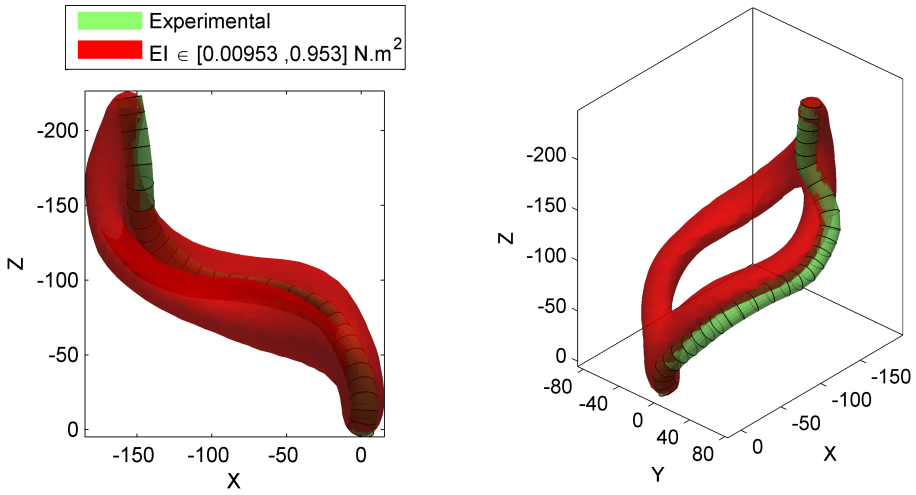

Figure 26: Volume swept by the cable in the final configuration for a varying *EI* - sample 1.

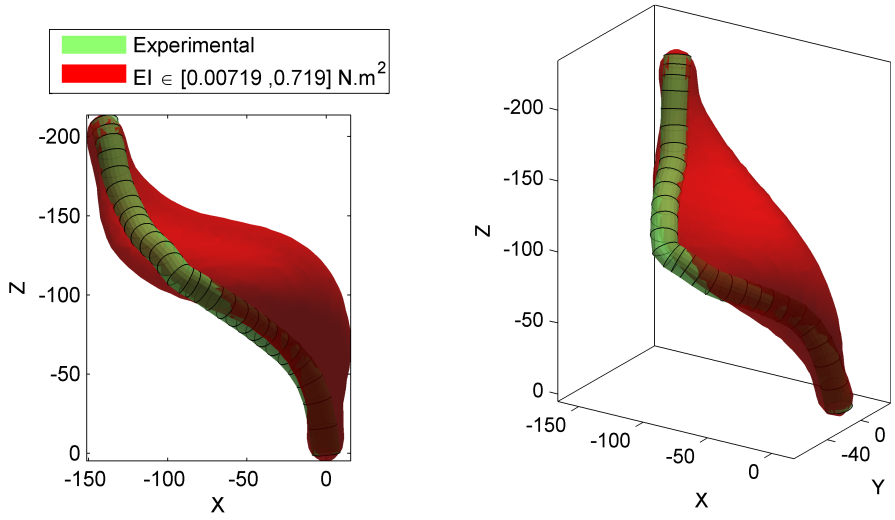

Figure 27: Volume swept by the cable in the final configuration for a varying *EI* - sample 3.

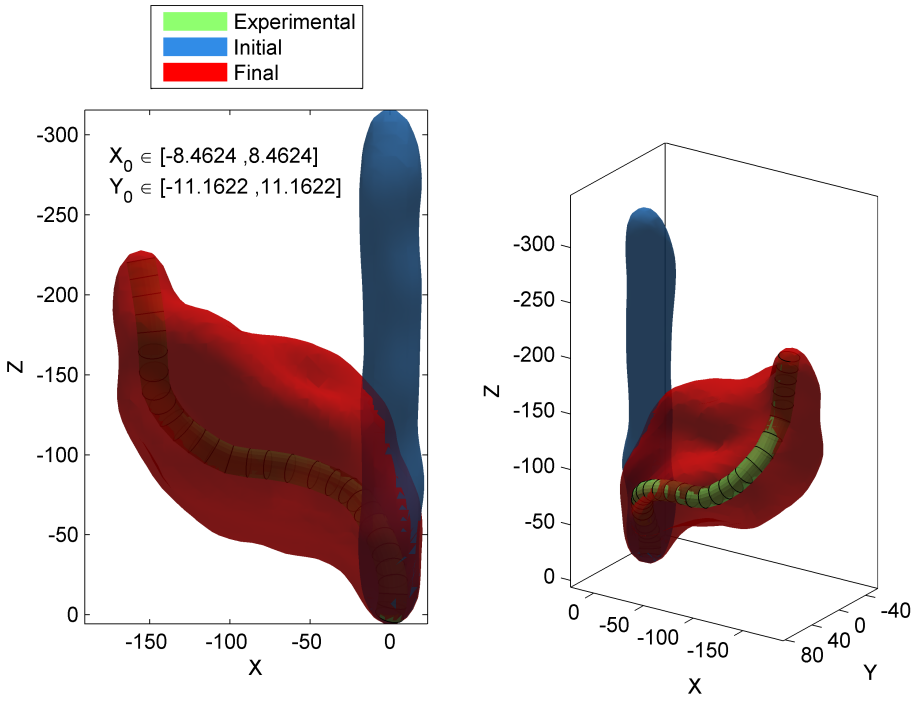

Figure 28: Volume swept by the cable in the final configuration for a varying initial geometry - sample 1.

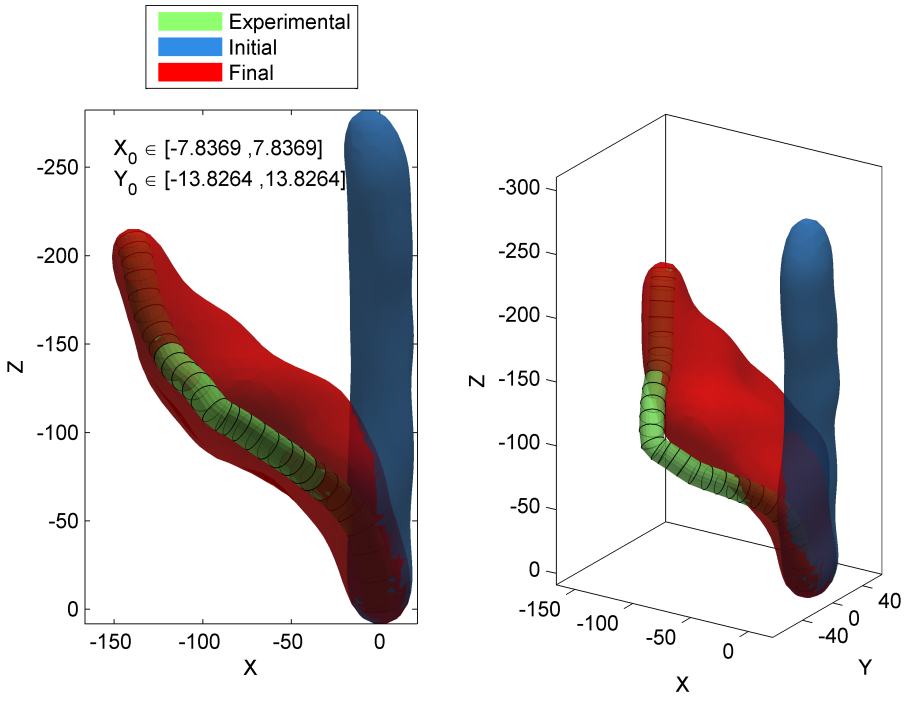

Figure 29: Volume swept by the cable in the final configuration for a varying initial geometry - sample 3.